Revision #2

Density Functional investigation of the thermo-physical and thermo-chemical properties of *2M$_1$* Muscovite

Gianfranco Ulian and Giovanni Valdrè*

Centro di Ricerca Interdisciplinare di Biomineralogia, Cristallografia e Biomateriali, Dipartimento di Scienze Biologiche, Geologiche e Ambientali, Università degli Studi di Bologna, Piazza di Porta San Donato 1, 40126 Bologna, Italy

E-mail: giovanni.valdre@unibo.it, Phone: +39-051-2094943, Fax: +39-051-2094943

Abstract

In the present study, we computed the thermo-chemical and thermo-physical properties of the 2*M$_1$* polytype of muscovite in the 0 – 10 GPa and 0 – 900 K ranges, using the hybrid DFT/B3LYP-D* density functional, corrected to take into account dispersive forces, and by using the quasi-harmonic approximation. The bulk modulus K_{T0} of muscovite, its first derivative K' and the unit-cell volume at zero pressure V_0 at 298.15 K, calculated using a third-order Birch-Murnaghan equation of state, were K_{T0} = 59.93 GPa, K' = 7.84 and V_0 = 940.6 Å^3. Our theoretical data are in good agreement with previous experimental results obtained by X-ray diffraction. Thermal bulk moduli, K_T, thermal expansion coefficients, α_T, and heat capacity at different *P,T* conditions are given, which could be useful in both geophysical and technological applications. The results of this kind of analysis can be used in the study of the thermodynamic properties of solid phases at physical conditions that are difficult to obtain during experimental procedures, especially under controlled high pressures and temperatures.

Keywords DFT, Quasi-harmonic approximation, Muscovite, Phonons, Thermal equation of state, Thermochemistry

INTRODUCTION

White dioctahedral micas (2:1 phyllosilicates) play a crucial role in most petrogenetic processes, in both magmatic and low- and medium-pressure metamorphic environments. For example, muscovite commonly occurs in metamorphic rocks and has been used as marker to estimate the *P*-*T* conditions of crystallization. Among the physical properties of interest, one of the most important parameters is the equation of state, which is the pressure- and temperature-dependence of the mineral unit-cell volume. Such equation is necessary for calculating the *P*-*T* conditions of mineral reactions. Understanding the mineral thermoelastic behavior is important to provide a reliable basis for interpretation and prediction of phase equilibria, as they are used as geothermometers and geobarometers (Guidotti and Sassi, 1976; Putnis, 1992; Guidotti et al., 1994; Guidotti and Sassi, 2002). To a first approximation, the rock-forming white micas can be described as crystalline solutions among the three end-members: muscovite (Ms), paragonite (Pg) and margarite (Mg). In the past, researchers attempted to use the partitioning of Na and K between coexisting muscovite and paragonite as a geothermometer (Guidotti and Sassi 1976). However, difficulties arose from using solvus curves not accurate enough to model the thermodynamic properties of these two micas. In fact, the exact shape of the solvus, and how it changes as a function of pressure and temperature are still not well known.

Many experimental studies contributed to the knowledge of the molar volumes of muscovite-2*M*1 polytype and of their variation with *P* (Comodi and Zanazzi, 1995; 1997) and *T* (Symmes 1986; Guggenheim et al. 1987; Catti et al. 1989; Comodi et al., 2002). These data allowed a definition of an approximate *P–V–T* equation of state for K- and Na-dioctahedral micas. However, these are only an indication of volumetric behaviour at the boundaries of the *P–T* conditions achieved in rocks in the Earth's crust. To determine more accurately the behaviour of muscovite–paragonite micas it is essential to verify if there are any ''non-linear effects'' when both *P* and *T* are high. If the effects of *P* and *T* on the volumetric properties of muscovite–paragonite micas were precisely known for the

full range of *P–T* conditions of geologic interest, it would be possible to accurately calculate effects on the muscovite–paragonite solvus. Relatively small changes in excess molar volume could have significant effect on solvus limb positions, particularly in the 600 to 700 °C range.

However, it is often difficult to obtain the equation of state, especially in natural mineral samples, because they present a series of both physical and chemical internal heterogeneities (cation order/disorder, morphological, crystal-chemical, and crystal-physical variations) which hinder a well-constrained evaluation of the physical properties (Mondol et al., 2008). Furthermore, obtaining experimentally the simultaneous pressure and thermal (*P-T*) behavior of a mineral is still a difficult task, which requires complex and expensive apparatuses.

In recent years, the adoption of accurate quantum mechanical approaches increased the knowledge on minerals. Such computational methods can provide reliable crystal structures, subsequently used to yield both the elastic and thermal properties by varying the mineral unit cell and using the quasi-harmonic approximation, respectively (Militzer et al., 2011; Ortega-Castro et al., 2010; Ottonello et al., 2010; Ottonello et al., 2009b; Prencipe et al., 2011; Stixrude, 2002). These methods provide results that can help to explain the thermo-chemical and thermo-physical behavior of minerals and aid interpretations of the seismologic data.

Muscovite presents an interesting challenge to computational mineralogists, because its structure is composed by tetrahedral-octahedral-tetrahedral (T-O-T) layers with potassium in the interlayer (see the structure of muscovite reported in Fig. 1). The simulation parameters should be chosen carefully when dealing with micas, because two directions of the mineral are dominated by covalent bonds (within the TOT layers), while the third direction exhibits an interplay of both van der Waals forces (between the layers) and strong ionic interactions due to the interlayer cations.

To the authors' knowledge, there is only one quantum mechanical simulation of the muscovite equation of state reported in literature by Ortega-Castro et al. (2010). That study was performed in athermal conditions, and the authors employed a Density Functional Theory (DFT) approach using the generalized gradient approximation (GGA) PBE functional, numeric atomic orbitals and norm

conserving pseudopotentials. Very recently, Hernandez-Haro and co-workers (2013) presented a DFT investigation on the elastic constants of the muscovite-paragonite mineral series, employing the same computational methods adopted by Ortega-Castro et al. (2010). The authors studied the effect of the K and Na content in the crystal lattice on the second order elastic constant tensor. Militzer et al. (2011) also calculated the isothermal elastic constants at 0 K of muscovite using DFT and looked at the effect of Al-Si cation disorder in the crystal structure. However, in both works the authors did not consider the contribution of the dispersive forces acting between the TOT layers, and the thermal effects on the mineral elastic properties.

The aim of our work is a further step in the knowledge of muscovite equation of state. We present a detailed theoretical simulation of the muscovite-$2M_1$ polytype of ideal chemical formula $KAl_2(AlSi_3)O_{10}(OH)_2$ to provide the thermal equation of state, the thermo-physical and thermo-chemical properties of the mineral, taking into account the dispersive force contribution. We employed the DFT/B3LYP-D* functional (dispersive forces corrected) and an all-electron localized Gaussian-type orbital basis set. This approach is known to provide very accurate structural and energy results of phyllosilicates, data required for a correct calculation of mineral physical-chemical properties (Ulian et al., 2013). First, we geometrically optimized the muscovite unit-cell and then compared the result to experimental and theoretical data available in literature. Secondly, the Muscovite athermal equation of state is obtained by varying the unit-cell volume and finally, using the quasi-harmonic approximation described by Anderson (1995), we calculated the thermo-mechanical and thermo-chemical properties of muscovite, as done in a previous work on talc (Ulian et al., 2014; Ulian and Valdrè, 2014). Thermal bulk moduli, K_T, thermal expansion coefficients, α_T, and heat capacity (isochoric, C_V, and isobaric, C_P) at different P-T conditions are provided, which could be useful in both geophysical and technological applications. For example, muscovite is currently used in resistors (Haynes, 2014) and in other electronic devices (Jin, 2011; Saito and Yamaguchi, 2009), in paints (Kalendova et al., 2010), and as additive in ceramics tailored for fuel cells (Liaw et al., 2011). Previous studied of Hsieh and co-workers (2009) showed that the thermal

conductivity of muscovite can be tuned by pressure. Heat capacity at constant pressure is finally compared to available experimental data of differential scanning calorimetry obtained by Robie et al. (1976).

COMPUTATIONAL DETAILS

Generality. We adopted the Becke three-parameter hybrid exchange functional (Becke, 1993) in combination with the gradient-corrected correlation functional of Lee, Yang, and Parr (Lee et al., 1988) for all calculations (B3LYP). The exchange–correlation contribution is the result of a numerical integration of the electron density and its gradient, and we calculated it over a pruned grid of 75 points and 974 angular points obtained from the Gauss–Legendre quadrature and Lebedev schemes (Prencipe et al., 2004). This represents a good compromise between accuracy and cost of calculation for geometry optimization and vibrational frequencies. The values of the tolerances that control the Coulomb and exchange series are the default provided by CRYSTAL09, but we increased the pseudo-overlap parameter to stabilize the self-consistent bahavior during unit-cell deformations. The Hamiltonian matrix has been diagonalized (Monkhorst and Pack, 1976) using a 4×4×4 k-mesh, which leads to 36 reciprocal lattice points. We chose this sampling grid to perform a better sampling along the **c**-axis direction, due to the mixed ionic/dispersive forces acting in that direction.

Within the CRYSTAL code, multi-electron wave functions are described by linear combination of crystalline orbitals (CO), expanded in terms of Gaussian-type orbital (GTO) basis sets. For all the calculations, oxygen has been described by a 8-411d11G basis sets, silicon by a 88-31G* (Nada et al., 1996) and hydrogen by a 3-1p1G basis set (Gatti et al., 1994). We had employed them with good results in our previous investigations of the structure and mechanical behavior of talc (Ulian et al., 2013; 2014). Aluminum and potassium atoms are described by a 8-511d1G (Catti et al., 1994b) and a 86-511G (Dovesi et al., 1991) basis sets, respectively. The chosen basis sets are well balanced

and, in particular the one of the hydrogen atom, allows accurate calculations in both molecular and crystal structures with sustainable computational costs.

We optimized lattice constants and internal coordinates within the same run using the analytical gradient method for the atomic positions and a numerical gradient for the unit-cell parameters. The Hessian matrix is upgraded with the Broyden–Fletcher–Goldfarb–Shanno algorithm (Broyden, 1970a; Broyden, 1970b; Fletcher, 1970; Goldfarb, 1970; Shanno, 1970). The tolerances for the maximum allowed gradient and the maximum atomic displacement for considering the geometry as converged have been set to $6 \cdot 10^{-5}$ hartree bohr^{-1} and $6 \cdot 10^{-5}$ Å, respectively.

In periodic systems and within the harmonic approximation, the phonon frequencies at Γ-point are evaluated diagonalising the central zone ($k = 0$) mass-weighted Hessian matrix:

$$W_{ij}(k=0) = \sum_G \frac{H_{ij}^{0G}}{\sqrt{M_i M_j}} \quad (1)$$

H_{ij}^{0G} represents the second derivative of the electronic and nuclear repulsion energy E evaluated at equilibrium **u=0** with respect to the displacement of atom A in cell 0 ($u_i = x_i - x_i^*$) and displacement of atom B in neighbouring cells G ($u_j = x_j - x_j^*$) from their equilibrium position x_i^*, x_j^*:

$$\sum_G H_{ij}^{0G} = \sum_G \left[\frac{\partial^2 E}{\partial u_i^0 \partial u_j^G} \right]_0 \qquad i = 1,...,3N; \quad j = 1,...,3N \quad (2)$$

M_i and M_j are the mass of the atoms associated to the i-th and j-th coordinates, respectively.

The calculation of the Hessian at equilibrium is made by the analytical evaluation of the energy first derivatives, Φ_j of E with respect to the atomic displacements:

$$\Phi_j = \sum_G v_j^G = \sum_G \frac{\partial E}{\partial u_j^G} \quad j = 1,...,3N \quad (3)$$

while second derivatives at **u = 0** (where all first derivatives are zero) are calculated numerically using a "two-point" formula:

$$\left[\frac{\partial \Phi_j}{\partial u_i^0}\right]_0 \approx \frac{\Phi_j\left(0,...,u_i^0,...,0\right)-\Phi_j\left(0,...,u_i^0,...,0\right)}{u_i^0} \quad (4)$$
$$i = 1,...,3N; \quad j = 1,...,3N$$

More details on the vibrational calculation made by CRYSTAL is beyond the scope of the present paper and can be found in specific literature (Pascale et al., 2004; Tosoni et al., 2005). The Hessian matrix eigenvalues provide the normal harmonic frequencies ω_h and it is obtained with 3N+1 self-consistent field and gradient calculations. This method can be quite demanding for large unit cells, but point symmetry facilitates a remarkable time saving, because only the lines of the Hessian matrix referring to irreducible atoms need to be generated. The tolerances were increased to obtain better results, TOLDEE = 10.

Density Functional Theory functionals, both generalized gradient approximation ones and their hybrid forms, often fails to adequately describe long-range dispersive interactions (Ulian et al., 2013). To overcome this problem, dispersive forces have been evaluated according to the semiempirical approach (DFT+D) suggested by Grimme (2006), which adds the following contribution to the calculated DFT energy:

$$E_{DISP} = -s_6 \sum_{\mathbf{g}} \sum_{i \neq j} f_{dump}\left(R_{ij,\mathbf{g}}^6\right) \frac{C_6^i C_6^j}{R_{ij,\mathbf{g}}^6} \quad (5)$$

$$f_{dump} = \frac{1}{1 + e^{-d\left(R_{ij,\mathbf{g}}/R_{vdw}-1\right)}}$$

The summation over all atom pairs *ij* and **g** lattice vectors excludes the self- interaction contribution ($i = j$) for every **g**. The parameters C_6^i represent the dispersion coefficient for the atom *I*; $R_{ij,\mathbf{g}}$ is the interatomic distance between atom *i* in the reference cell and atom *j* in the neighbouring cells at distance |**g**| and s_6 is a functional-dependent scaling factor. We employed the C_6^i parameters reported in the work of Grimme (2006), which were obtained from atomic ionization

potentials (I_p) and static dipole polarizabilities (α) according to the formula $C_6^i = 0.05NI_p^i\alpha^i$, where N depends on atom row in the periodic table. The function f_{dump} is used to dump the energy correction to avoid double counting of short-range contributions and depends on the sum of atomic van der Waals radii (R_{vdw}) and on a steepness parameter (d = 20). According to results previously reported in literature (Civalleri et al., 2008), which show that the E_{DISP} correction tends to overestimate cohesive energy in solid crystals, the original B3LYP+D parameters were modified. We set s_6 to 1, the hydrogen atom van der Waals radius R_{vdw}(H) to 1.30 and the heavier atoms van der Waals radii were scaled by a factor 1.05, correction called B3LYP-D*, named by Civalleri et al. (2008). The same approach was adopted with good results in a previous work on talc (Ulian et al., 2013).

Thermomechanical and thermochemical properties. We calculated the total pressures, bulk moduli, thermal expansion coefficients and heat capacity in the limit of the quasi-harmonic approximation described by (Anderson, 1995). The approach is based on the Grüneisen's mode-γ parameters, namely the evaluation of unit cell volume dependence of the vibrational normal mode frequencies, calculated at Γ point. Due to the limited computational resources, we did not take into account dispersion effects in the muscovite phonon spectra at different pressures. However, the number of atoms in the unit cell, and the corresponding number of vibrational frequencies at Γ point, are sufficiently large and the corresponding Grüneisen's parameters can be considered representative of the whole set of parameters. In previous works (Ottonello et al., 2010; Ottonello et al., 2009a; Ottonello et al., 2009b; Prencipe et al., 2011; Ulian and Valdrè, 2014) the dispersion effects were neglected, but the thermomechanical and thermochemical properties were correctly estimated for minerals with unit cell smaller than that of muscovite. Indeed, thermodynamic properties, which are obtained as averages over the relevant quantities at the atomic level, can reliably be derived even without a detailed knowledge of the phonon density of state (Kieffer, 1979a).

198 The pressure, at each unit cell volume and temperature, is related to the Helmholtz free energy F
199 of a solid insulator (Anderson, 1995)

200 $$F = E_{ST}(V) + F_{VIB}(V,T) \quad (6)$$

201 where E_{ST} is the potential of a static lattice at absolute zero (athermal limit) and F_{VIB} is the
202 vibrational energy related to the thermal motion of the atoms.

203 The pressure can be obtained by the volume first derivative of Eq.(6)

204 $$P = -\left(\frac{\partial F}{\partial V}\right)_T = -\left(\frac{\partial E_{ST}}{\partial V}\right)_{T=0} + \left(\frac{\partial F_{VIB}}{\partial V}\right)_T \quad (7)$$

205 Using the energy partition principle, the expression that relates the pressure at each volume and
206 temperature is given by:

207 $$P = -\left(\frac{\partial E_{ST}}{\partial V}\right)_{T=0} + \frac{kT}{2V}\sum_{i=1}^{3n-3}\gamma_i X_i + \frac{kT}{V}\sum_{i=1}^{3n-3} n_i(\nu_i,T)\gamma_i X_i \quad (8)$$

208 where

209 $$n_i(\nu_i,T) = \frac{1}{e^{X_i}-1} \quad (9)$$

210 and $X_i = h\nu_i/kT$, h and k are the Planck's and Boltzmann's constants, respectively, ν_i is the
211 vibrational frequency of the ith normal mode and n_i is the Bose-Einstein distribution applied to the
212 phonon gas. The Grüneisen's mode-γ parameter is defined as

213 $$\gamma_i = -\frac{\partial \ln \nu_i}{\partial \ln V} = -\frac{V}{\nu_i}\frac{\partial \nu_i}{\partial V} \quad (10)$$

214 and were estimated by the analytical derivatives with respect to V of quadratic polynomials fitting
215 the numerically determined $\gamma_i(V)$ curves. The total pressure given by Eq.(8) is the sum of three
216 contributions: the first one is the *static* pressure $P_{st}(V)$; the second one is the *zero point* pressure
217 $P_{zp}(V)$ and the third one is the *thermal* pressure $P_{th}(V,T)$.

218 We calculated the static pressure $P_{st}(V)$values by interpolation of the $E_{st}(V)$ curve by Legendre's
219 polynomials up the third order and obtaining the static pressures as derivatives of the resulting
220 analytical curves. The *vibrational* pressure, namely $P_{vib}(V,T) = P_{zp}(V) + P_{th}(V,T)$, was obtained

directly from Eqs. (8) and (9). As observed by Prencipe et al. (2011) this method would implicitly assume the constancy of the Grüneisen's parameters as the cell volume is reduced in a finite interval. However we calculated the volume dependence of the mode-γparameters.

With the set of *P(V,T)* data obtained as described above, we derived the volume at zero pressure (V_0), the bulk modulus (K_T) and its first derivative with respect to *P* (*K'*) using a third order Birch-Murnaghan equation of state (BM3) (Birch, 1947):

$$P_{BM3} = \frac{3}{2}K_T\left[\left(\frac{V}{V_0}\right)^{-7/3} - \left(\frac{V}{V_0}\right)^{-5/3}\right]\left\{1-\frac{3}{4}(4-K')\left[\left(\frac{V}{V_0}\right)^{-2/3}-1\right]\right\}+P_0 \qquad (11)$$

with V_0 the volume at reference pressure P_0 (P_0 = 0.0 GPa). We made the root mean square fitting of *P* as a function of *V* at each temperature with the EOS-FIT5.2 software (Angel, 2001).

The thermal expansion coefficient (α_T) at any given cell volume (pressure), as a function of *T*, is obtained by direct evaluation of the $\alpha_T K_T$ product (Anderson, 1995):

$$\alpha_T K_T = \frac{R}{ZV}\sum_{i=4}^{3n}\gamma_i e^{X_i}\left(\frac{X_i}{e^{X_i}-1}\right)^2 \qquad (12)$$

where K_T at each *P-T* condition is calculated from Eq.(11).

The isochoric heat capacity as a function of *T* of a solid insulator can be expressed by (Anderson, 1995)

$$C_V = \frac{R}{Z}\sum_{i=4}^{3n}\frac{X_i^2 e^{X_i}}{\left(e^{X_i}-1\right)^2} \qquad (13)$$

The specific heat at constant pressure (C_P) can be obtained from the relationship

$$C_P = C_V + T\alpha_T^2 K_{T,P} V_{P,T} \qquad (14)$$

where $V_{P,T}$ is the cell volume at pressure *P* and temperature *T*, respectively. It is worth noting that the isochoric specific heat expression in Eq. (13) does not include the acoustic mode contribution described by the Kieffer's sinusoidal dispersion (Kieffer, 1979b). This contribution is calculated from the acoustic (seismic) wave velocities within the mineral, which are in turn derived from the

second order elastic constants (SOEC). We did not calculate the muscovite SOEC, because, as observed in our previous work on talc (Ulian and Valdrè, 2014), the contribution from the acoustic branch is very small at $T > 300$ K, consequently the description of the thermochemical properties is adequately described by the sole optical modes, and a saving is made on the computational costs.

RESULTS AND DISCUSSION

Geometry. The starting muscovite structure was taken from XRD refinement data of Guggenheim et al. (1987), belonging to the *C2/c* space group. However, in our simulations we employed a lower-symmetry space group, $P\bar{1}$, which could break the monoclinic symmetry of muscovite. This choice was made for two reasons: the first one regards testing the stability of the quantum mechanical approach; the second one is letting the mineral crystallographic cell freely relax during compression (*vide infra*). Hydrogen atoms location is similar to the one of pyrophyllite structure, with O-H bond direction canted by about 30° on the [001] direction. Oxygen atoms are subdivided in three groups: apical [O^a or O(a)] shared between Si and Al; hydroxyl [O^h or O(h)]; basal [O^b or O(b)] shared between silica tetrahedrons. Aluminum atoms substitute silicon ones in the tetrahedral layer so as to maintain the unit-cell symmetry. Albeit this choice does not consider all possible aluminum distribution in the real mineral, it is a good starting model to be compared to experimental observations. See the stick and ball graphical representation of muscovite reported in Fig. 2.

The optimized results of the structure of muscovite obtained by GTO/B3LYP-D* approach are described in details in Table 1, in comparison with a series of X-Ray and neutron diffraction refinements (Brigatti et al., 1998; Gatta et al., 2011; Guggenheim et al., 1987) and very recent theoretical results reported in literature (Hernandez-Haro et al., 2013). Our data are in general agreement with all those obtained experimentally, reported in Table 1, with small deviations due to the temperature analysis and mineral compositions. However, in the following we discuss and compare our structural theoretical results, calculated at T = 0 K, with Neutron Diffraction ones (Gatta et al., 2011), obtained at similar temperature (T = 20 K).

It can be seen that lattice parameters and bond lengths (internal geometry) are in good agreement to those of Gatta et al. (2011), with only a small over-estimation of the cell volume (+0.6%). In particular, the description of the **c**-axis is accurate, although with a small underestimation of about 0.7%. It is worth to note that, albeit the adopted space group breaks the monoclinic symmetry of muscovite, the deviations from ideal α and γ angles (90°) are less than 0.3%. The interlayer thickness, I (see Fig.1), is very close to that reported experimentally. This observation suggests the Grimme's semi-empirical correction for dispersive forces provides an adequate description of the energy and geometry of the muscovite mineral.

Athermal equation of state and internal geometry variations. We report in Table 2 the muscovite relaxed lattice parameters at the athermal limit. We found that the relationship between the muscovite energy E_{st} at different volumes V, i.e. $E_{st}(V)$ curve, is well described by a 3rd-order polynomial equation with parameters $p_1 = -3.509 \cdot 10^{-8}$, $p_2 = 1.052 \cdot 10^{-4}$, $p_3 = -1.046 \cdot 10^{-1}$ and $p_4 = 3.449 \cdot 10^{+1}$ ($R^2 = 0.999995$). We were able to obtain the static pressure related to each volume $P_{st}(V)$ by derivation of the $E_{st}(V)$ curve, according to Eq.(7). A graphical representation of the $E_{st}(V)$ and $P_{st}(V)$ trends are shown in Figs. 3a,b, respectively.

Next step is the calculation of muscovite bulk modulus at 0 K (K_{T0}), its pressure first derivative (K') and the volume at zero pressure (V_0) by fitting the volume *vs*. P_{st} data using BM3 equation of state. The refined elastic parameters are $V_0 = 926.86(38)$ Å^3, $K_{T0} = 64.2(1.2)$ GPa and $K' = 7.98(33)$.

In Fig.4a,b we report the evolution of volume and lattice parameters at different pressure, respectively. Regarding the compressive regime ($P > 0$ GPa), the calculated trend is monotonic (Fig.4a). It is graphically clear that muscovite deformation exhibits a strongly anisotropic behavior, with smaller variations for *a* and *b* cell parameters than for *c*. It is possible to describe the observed anisotropy by calculating the axial bulk moduli with a linear BM3 fit (Angel, 2001) on the lattice parameters at different pressures. The obtained refined data, after the BM3 fit, for the *a*, *b* and *c* axis were, respectively: $a_0 = 5.1975 \pm 0.0148$ Å, $K_{T0}(a) = 136.95 \pm 1.12$ GPa and $K'(a) = 5.27 \pm 0.25$; $b_0 =$

9.0392±0.0935 Å, $K_{T0}(b)$ = 118.25±1.01 GPa and $K'(b)$ = 5.01±0.22; c_0 = 19.8495±0.1602 Å, $K_{T0}(c)$ = 30.27±0.36 GPa and $K'(c)$ = 6.60±0.12. Note that the lattice parameters a_0, b_0 and c_0 are slightly different from those reported in Table 1, obtained by structural optimization, because of the BM3 fit. The axial compressibilities, described as $\beta = 1/3K_{T0}$, are accordingly in the ratio β(a): β(b): β(c) = 1.000 : 1.158 : 4.525. This result suggests that the covalent bonds in the dioctahedral TOT layers are less compressible than the interlayer dominated by electrostatic and van der Waals forces (*c* direction).

Regarding the internal geometry of muscovite, the pressure affects the size, shape and orientation of the coordination polyhedrons. While the thickness of the TOT layer is almost non-affected by pressure (-2.0%), the interlayer thickness I shrinks of about 15% at 10 GPa (Fig. S1 – Supplementary Materials), in agreement with the axial moduli. The pressure increase produces a volume reduction in both SiO_4/AlO_4 tetrahedra and AlO_6 octahedra of about 3-4%. The mean Si – O and Al – O bond lengths are contracted by 0.9% and 1.3%, respectively, from 0 to 10 GPa. In the case of Si tetrahedron, the reduction is higher for the apical oxygen than for the basal ones. In both cases, the bond length contraction removes some distortion in the tetrahedra and in the octahedra.

Another structural response to the compression is the increase of the tetrahedral rotation angle, which is defined as $\alpha = 1/2\left(\sum_{i=1}^{6}\left|\phi_i - 120°\right| \Big/ 6\right)$, where ϕ_i is the angle described by triples of basal oxygen atoms (Bailey, 1988; Ulian et al., 2014). The calculated value of α increases from 13.2° at 0 GPa to 14.6° at 10 GPa (see Fig.S2 – Supplementary Materials).

We did not observe any significant variation in O-H bond lengths in the pressure range investigated (0.962 Å at 0 GPa and 0.963 Å at 10 GPa), nor in their directions.

Our results are in line to those of Ortega-Castro et al. (2010) obtained in athermal conditions with generalized gradient approximation (GGA) and the Perdew-Burke-Ernzerhof (PBE) functional. The BM3 fit on *V(P)* data in the cited work is very similar to ours, albeit with small underestimations (K_{T0} = 60.1 GPa and K' = 7.3). However, it can be observed in Fig. 4a that our muscovite volumes

at different *P* are smaller than those obtained by Ortega-Castro and co-workers (2010). Hernández-Haro et al. (2013) derived with DFT simulations at T = 0 K the bulk modulus of end-member muscovite from the elastic constants, obtaining K_{T0} = 68.4 GPa. The small difference between our results and the previous ones is imputable to at least two reasons. First, in our simulations we adopted an all-electron GTO basis set with hybrid B3LYP functional, including a correction for dispersive forces, whereas in both previous works (Hernandez-Haro et al., 2013; Ortega-Castro et al., 2010) the authors used a GGA functional (PBE) with norm conserving pseudopotentials. The generalized gradient approximation tends to soften bonds and consequently the bulk modulus, which explains the low K_{T0} value and the large volumes of Ortega-Castro et al. (2010). Secondly, we observed in a previous work on talc (Ulian et al., 2014) that the bulk modulus obtained from the elastic stiffness is very sensitive on both the way of its calculation (e.g. Reuss bound, Voigth bound, etc.) and on the anisotropic behavior of the mineral.

Compared to previous theoretical results on similar and other layered hydrous silicates, our muscovite model exhibits a higher bulk modulus than both TOT minerals without interlayer cations, such as talc (Mainprice et al., 2008), and TO structures, for example serpentine (Mookherjee and Stixrude, 2009), antigorite (Capitani et al., 2009; Mookherjee and Capitani, 2011; Capitani and Stixrude, 2012). On one hand, in the case of talc the absence of interlayer cations favors the compression along the **c**-axis direction, resulting in a fairly low bulk modulus (K_{T0} = 42.1 GPa). On the other hand, in TO minerals characterized by half-waves and reversals of the T-O sheets (serpentine group) the elastic softening is related to the adjustment of the relative misfit between the tetrahedral and octahedral sheets (Mookherjee and Capitani, 2011). Considering other micas, our muscovite model presents a stiffer nature than the phlogopite calculated by Chheda et al. (2014) with GGA functional. Phlogopite is the Mg-trioctahedral equivalent of muscovite, and the lower bulk modulus may be due to the difference in the octahedral sheet composition. Finally, our muscovite model presents a K_{T0} value lower than the one calculated for chlorite (Mookherjee and

Mainprice, 2014), because the latter presents a brucite-like sheet sandwiched between talc-like TOT layers , which is less compressible than the interlayer with potassium cations.

Thermomechanical and thermochemical properties. As explained in the computational method section, we calculated the muscovite thermal properties from the mineral vibrational features using the quasi-harmonic approximation.

There are 84 atoms in the muscovite unit-cell, which result in 84 x 3 = 252 normal modes, three of them related to translation of the whole unit-cell. The remaining 249 optic modes are subdivided in the following irreducible representations:

$$\Gamma_{tot} = 126A_g + 123A_u$$

Modes with A_g symmetry are Raman-active, while A_u ones are IR-active, but both do not exhibit degeneracies. For each optic normal mode ($3n - 3$) we determined the mode-γ parameters. Between 30 and 1200 cm^{-1} (see Fig. 5a), all parameters are positive and, according to Eq.(8), they contribute positively to the total pressure. In this frequency range, only one vibrational mode is associated with a small negative γ. Above 1200 cm^{-1} the mode-γ are negative ($\gamma \approx -0.1$) and give negative contribution to the pressure values. The mean Grüneisen's parameter ($\overline{\gamma}$) is equal to 0.67. We reported the results and the mode-gammas for each frequency at zero pressure in Table S1 (Supplementary material).

Using Eq.(11) we calculated the thermal contribution to athermal pressure values in the range 10 – 900 K. To help the interested readers in better understanding how the quasi-harmonic approximation works, we plotted in Fig. 5b the static (P_{st}), zero point (P_{zp}) and thermal (P_{th}) pressure contribution to P = 0 GPa total pressure as a function of temperature. The zero point pressure is almost constant, as it is a function of the sole volume. The thermal pressure increases, as the Grüneisen's parameters are almost all positive. Since there is an external pressure constrain (0 GPa), to maintain the equilibrium the static pressure mirrors the thermal pressure behavior, with a shift in pressure due to P_{zp}.

In Fig. 6a we show the *V(P)* values obtained at 298 K, alongside experimental data from powder XRD (Comodi et al., 2002; Curetti et al., 2006). There is a good agreement with the volumetric behavior of muscovite in the range 0 – 10 GPa. We noticed also that the comparison is more favorable with the data of Curetti and co-workers (2006) than with that of Comodi et al. (2002), despite the very small overestimation observed with the B3LYP-D* approach. The slight difference between the two experimental results and our set of data resides in the chemical composition and the physical preparation of the muscovite sample. While both powdered samples exhibit a wide presence of substitutional defects, such as Mg and Fe^{3+} in the octahedral sheet, our model represents an "ideally" pure muscovite mineral. Furthermore, the nature of the experimentally analyzed samples, namely powdered Ms, is formally different from our model, realized with periodic boundary conditions (hence, "single-crystal"). In fact, as observed in our previous work on talc (Ulian and Valdrè, 2014), it is expected that the results obtained from the quantum mechanical approach fit better with those obtained experimentally on a single-crystal specimen. In Fig. 6b we reported a three-dimensional plot of the *V(P,T)* data in the range 10 – 900 K.

With the pressure and temperature data, we fitted the results by the third-order Birch-Murnaghan equation of state for each *P-T* condition. The results, K_T, *K'* and V_T obtained in the pressure range 0 – 10 GPa and between 10 – 900 K are reported in Tables S2, S3 and S4 (Supplementary Materials), respectively. At room temperature (T = 298 K) and 0 GPa the refined equation of state parameters are K_{T0} = 59.93 GPa, *K'* = 7.84 and V_0 = 940.6 Å^3. These data well match those obtained in previous powder XRD experiments at T = 298 K, K_{T0} = 57.3 GPa, *K'* = 6.97 and V_0 = 938.9 Å^3 in the work of Curetti et al. (2002) and K_{T0} = 57.0 GPa and V_0 = 933.0 Å^3 in the investigation of Comodi et al. (2002). We also compared our theoretical BM3 results at 573, 723 and 873 K with the corresponding experimental values at the same temperatures of the work of Comodi et al. (2002) (see Table 3). The theoretical BM3 fitting for each isotherm is in reasonable agreement with experimental data, with a slight overestimation of both bulk moduli (+3.8%) and unit cell volume at zero pressure (+1.3%). This systematic shift suggests that the quasi-harmonic approximation

396 describes well the thermomechanical behavior of muscovite at high temperature and the deviations
397 could be imputable to the different composition and preparation in the experimental sample, as
398 previously explained.

399 From the calculated bulk modulus at different temperatures, we obtained its thermal dependency
400 at 0 GPa, $(\partial K_T/\partial T)_P$ = -0.0158 GPa K^{-1}, which is close to the experimental result of Comodi et al.
401 (2002) that is $(\partial K_T/\partial T)_P$ = –0.0146 GPa K^{-1}.

402 The $\alpha_T K_T$ product attains the value of 2.39·10^{-3} GPa/K in the 100 – 900 K range and reaches a
403 constant value of 2.48·10^{-3} GPa/K at very high temperatures (see Fig. 7a). A three-dimensional plot
404 of the $\alpha_T K_T$ product in the 0 – 10 GPa and 10 – 900 K ranges is reported in Fig. S3a
405 (Supplementary Materials).

406 We calculated the thermal expansion coefficient (α_T) from the $\alpha_T K_T$ product by the thermal bulk
407 modulus previously obtained. We plotted the $\alpha(T)_P$ values at pressures 0, 5 and 10 GPa in Fig. 7b. It
408 is possible to observe that the thermal expansion coefficient decreases with pressure increase.
409 There is a good agreement between the theoretical value at standard P and T (α_T = 3.34 · 10^{-5} K^{-1})
410 and those of different experimental results obtained in the same conditions: α_T = 3.57 · 10^{-5} K^{-1}
411 (Comodi et al., 2002) and α_T = 3.54 · 10^{-5} K^{-1} (Guggenheim et al., 1987). A three-dimensional plot
412 in the 0 – 10 GPa and 10 – 900 K ranges is reported in Fig. S3b (Supplementary Materials).

413 The isochoric and isobaric heat capacities were calculated with Eqs. (13) and (14), respectively
414 (see Fig. 7c and Fig. S3c – Supplementary Materials). It was observed that C_V attains the Dulong-
415 Petit limit (Ottonello et al., 2009a;b) at high temperatures. For both isochoric and isobaric specific
416 heat, it can be observed a decrease of their values by increasing pressure. The C_P vs. T data are
417 fitted in the range 298.15 – 900K according to the form of a Haas–Fisher polynomial expression
418 (Haas and Fisher, 1976), which is:

419 $$C_P = a + b \cdot T + c \cdot T^{-2} + d \cdot T^2 + e \cdot T^{-1/2} \quad (11)$$

The retrieved regression coefficients, $a = 8.2044 \cdot 10^{2}$, $b = -3.5759 \cdot 10^{-2}$, $c = 0.8976$, $d = 5.4382 \cdot 10^{-}5$ and $e = -8.5978 \cdot 10^{3}$, reproduce computed heat capacities with a mean error of about ± 0.26 J mol^{-1} K^{-1} and the summation of squared residuals over 13 values is 1.1.

Compared to experimental scanning calorimetric data of Robie et al. (1976), the calculated isobaric heat capacity in the range 10 – 380 K nicely fit the experimental results, albeit with a small deviation above room temperature.

IMPLICATIONS

The thermodynamic and thermoelastic properties of muscovite, and how they change as a function of pressure and temperature are still not well known. These properties are important for a reliable basis to the interpretation of phase equilibria. White dioctahedral micas play a fundamental role in most petrogenetic processes, in both magmatic and low- and medium-pressure metamorphic environments. Among the physical properties to estimate the *P-T* conditions of mineral stability, one of the most important function is the equation of state, which relates the unit-cell volume to the pressure and temperature. We reported in the present paper the thermal equation of state of muscovite, calculated by quantum mechanics. Furthermore, the proposed theoretical approach, based on a DFT/B3LYP-D* quantum mechanics modelling, with semi-empirical correction for dispersive force, and using the quasi-harmonic treatment to include the thermal effects is promising for detailed structural, thermo-mechanical and thermo-chemical analysis of other phyllosilicates. The results of this kind of analysis find usefulness in the study of the thermodynamic properties of minerals at physical conditions that are difficult to obtain during experimental procedures, especially under controlled high pressures and temperatures.

REFERENCES CITED

Anderson, O.L. (1995) Equation of state of solids for geophysics and ceramic science. 405 p. Oxford University Press, New York, US.

Angel, R.J. (2001) EOS-FIT6.0. Computer Program (http://www.rossangel.com).

Bailey, S.W. (1988) Introduction, Hydrous Phyllosilicates. Reviews in Mineralogy & Geochemistry, 19, 1-8.

Becke, A.D. (1993) Density-Functional Thermochemistry .3. The Role of Exact Exchange. Journal of Chemical Physics, 98(7), 5648-5652.

Birch, F. (1947) Finite elastic strain of cubic crystal. Physical Review, 71, 809-824.

Brigatti, M.F., Frigieri, P., and Poppi, L. (1998) Crystal chemistry of Mg-, Fe-bearing muscovites-2M(1). American Mineralogist, 83(7-8), 775-785.

Broyden, C.G. (1970a) The convergence of a class of double-rank minimization algorithms 1. General considerations. IMA Journal of Applied Mathematics (Institute of Mathematics and Its Applications), 6(1), 76-90.

-. (1970b) The convergence of a class of double-rank minimization algorithms: 2. The new algorithm. IMA Journal of Applied Mathematics (Institute of Mathematics and Its Applications), 6(3), 222-231.

Burnham, C.W., and Radoslovich, E.W. (1964) Crystal structure of coexisting muscovite and paragonite. Carnegie Institute of Washington Year Book, 63, 232-236.

Capitani, G.C., and Stixrude, L. (2012) A first-principle investigation of antigorite up to 30 GPa: Structural behavior under compression. American Mineralogist, 97(7), 1177-1186.

Capitani, G.C., Stixrude, L., and Mellini, M. (2009) First-principles energetics and structural relaxation of antigorite. American Mineralogist, 94(8-9), 1271-1278.

Catti, M., Ferraris, G., Hull, S., and Pavese, A. (1994a) Powder Neutron-Diffraction Study of 2m1 Muscovite at Room Pressure and at 2 Gpa. European Journal of Mineralogy, 6(2), 171-178.

Catti, M., Ferraris, G., and Ivaldi, G. (1989) Thermal Strain Analysis in the Crystal-Structure of Muscovite at 700-Degrees-C. European Journal of Mineralogy, 1(5), 625-632.

Catti, M., Valerio, G., Dovesi, R., and Causa, M. (1994b) Quantum-mechanical calculation of the solid-state equilibrium MgO + alpha-Al_2O_3 $MgAl_2O_4$ (spinel) versus pressure. Physical Review B, 49(20), 14179-14187.

Chheda, T.D., Mookherjee, M., Mainprice, D., dos Santos, A.M., Molaison, J.J., Chantel, J., Manthilake, G., and Bassett, W.A. (2014) Structure and elasticity of phlogopite under compression: Geophysical implications. Physics of the Earth and Planetary Interiors, 233, 1-12.

Civalleri, B., Zicovich-Wilson, C.M., Valenzano, L., and Ugliengo, P. (2008) B3LYP augmented with an empirical dispersion term (B3LYP-D*) as applied to molecular crystals. CrystEngComm, 10(4), 405-410.

Comodi, P., Gatta, G.D., Zanazzi, P.F., Levy, D., and Crichton, W. (2002) Thermal equations of state of dioctahedral micas on the join muscovite-paragonite. Physics and Chemistry of Minerals, 29(8), 538-544.

Comodi, P., and Zanazzi, P.F. (1995) High-Pressure Structural Study of Muscovite. Physics and Chemistry of Minerals, 22(3), 170-177.

-. (1997) Pressure dependence of structural parameters of paragonite. Physics and Chemistry of Minerals, 24(4), 274-280.

Curetti, N., Levy, D., Pavese, A., and Ivaldi, G. (2006) Elastic properties and stability of coexisting 3T and 2M(1) phengite polytypes. Physics and Chemistry of Minerals, 32(10), 670-678.

Dovesi, R., Roetti, C., Freyria Fava, C., Prencipe, M., and Saunders, V.R. (1991) On the elastic properties of lithium, sodium an potassium oxide. An ab initio study. Chemical Physics, 156, 11-19.

Fletcher, R. (1970) A new approach to variable metric algorithms. The Computer Journal, 13(3), 317-322.

Gatta, G.D., McIntyre, G.J., Sassi, R., Rotiroti, N., and Pavese, A. (2011) Hydrogen-bond and cation partitioning in muscovite: A single-crystal neutron-diffraction study at 295 and 20 K. American Mineralogist, 96(1), 34-41.

Gatti, C., Saunders, V.R., and Roetti, C. (1994) Crystal-field effects on the topological properties of the electron-density in molecular-crystals - the case of urea. Journal of Chemical Physics, 101(12), 10686-10696.

Goldfarb, D. (1970) A family of variable-metric methods derived by variational means. Mathematics of Computation, 24, 23-26.

Grimme, S. (2006) Semiempirical GGA-type density functional constructed with a long-range dispersion correction. Journal of Computational Chemistry, 27(15), 1787-1799.

Guggenheim, S., Chang, Y.H., and Koster Van Groos, A.F. (1987) Muscovite dehydroxylation: high-temperature studies. American Mineralogist, 72(5-6), 537-550.

Guidotti, C.V., and Sassi, F.P. (1976) Muscovite as a petrogenetic indicator mineral in pelitic schists. Neues Jahrbuch fuer Mineralogie, Abhandlungen, 123, 97-142.

-. (2002) Constraints on studies of metamorphic K-Na white micas. Micas: Crystal Chemistry and Metamorphic Petrology, 46, 413-448.

Guidotti, C.V., Sassi, F.P., Sassi, R., and Blencoe, J.G. (1994) The Effects of Ferromagnesian Components on the Paragonite-Muscovite Solvus - a Semiquantitative Analysis Based on Chemical-Data for Natural Paragonite-Muscovite Pairs. Journal of Metamorphic Geology, 12(6), 779-788.

Haas, J.L., and Fisher, J.R. (1976) Simultaneous evaluation and correlation of thermodynamic data. American Journal of Science, 276, 525-545.

Hernandez-Haro, N., Ortega-Castro, J., Del Valle, C.P., Munoz-Santiburcio, D., Sainz-Diaz, C.I., and Hernandez-Laguna, A. (2013) Computational study of the elastic behavior of the 2M(1) muscovite-paragonite series. American Mineralogist, 98(4), 651-664.

Hsieh, W.-P., Chen, B., Li, J., Keblinski, P., and Cahill, D.G. (2009) Pressure tuning of the thermal conductivity of the layered muscovite crystal. Physical Review B, 80(18).

Jin, K.L. (2011) Electronic ondol panel equipment for use with loess board, has molding product, where the panel equipment and loess board are made of red clay, magnesium oxide, obsidian, muscovite and magnesium chloride. Jin K L.

Kalendova, A., Vesely, D., and Kalenda, P. (2010) Properties of paints with hematite coated muscovite and talc particles. Applied Clay Science, 48(4), 581-588.

Kieffer, S.W. (1979a) Thermodynamics and lattice vibrations of minerals - 2. vibrational characteristics of silicates. Reviews of Geophysics and Space Physics, 17(1), 20-34.

-. (1979b) Thermodynamics and lattice vibrations of minerals - 3. lattice dynamics and an approximation for minerals with application to simple substances and framework of silicates. Reviews of Geophysics and Space Physics, 17(1), 35-59.

Lee, C.T., Yang, W.T., and Parr, R.G. (1988) Development of the Colle-Salvetti Correlation-Energy Formula into a Functional of the Electron-Density. Physical Review B, 37(2), 785-789.

Liaw, D.-W., Tsai, C.-Y., and Wei, W.-C.J. (2011) Thermal insulation of muscovite/glass ceramic foam for solid oxide fuel cell. Journal of Power Sources, 196(19), 8012-8018.

Mainprice, D., Le Page, Y., Rodgers, J., and Jouanna, P. (2008) Ab initio elastic properties of talc from 0 to 12 GPa: Interpretation of seismic velocities at mantle pressures and prediction of auxetic behaviour at low pressure. Earth and Planetary Science Letters, 274(3-4), 327-338.

Militzer, B., Wenk, H.R., Stackhouse, S., and Stixrude, L. (2011) First-principles calculation of the elastic moduli of sheet silicates and their application to shale anisotropy. American Mineralogist, 96(1), 125-137.

Mondol, N.H., Jahren, J., and Bjørlykke, K. (2008) Elastic properties of clay minerals. Leading Edge (Tulsa, OK), 27(6), 758-770.

Monkhorst, H.J., and Pack, J.D. (1976) Special points for Brillouin-zone integrations. Physical Review B, 8, 5188-5192.

Mookherjee, M., and Redfern, S.A.T. (2002) A high-temperature Fourier transform infrared study of the interlayer and Si-O-stretching region in phengite-2M(1). Clay Minerals, 37(2), 323-336.

Mookherjee, M., and Capitani, G.C. (2011) Trench parallel anisotropy and large delay times: Elasticity and anisotropy of antigorite at high pressures. Geophysical Research Letters, 38.

Mookherjee, M., and Mainprice, D. (2014) Unusually large shear wave anisotropy for chlorite in subduction zone settings. Geophysical Research Letters, 41(5), 1506-1513.

Mookherjee, M., and Stixrude, L. (2009) Structure and elasticity of serpentine at high-pressure. Earth and Planetary Science Letters, 279(1-2), 11-19.

Nada, R., Nicholas, J.B., McCarthy, M.I., and Hess, A.C. (1996) Basis sets for ab initio periodic Hartree-Fock studies of zeolite/adsorbate interactions: He, Ne, and Ar in silica sodalite. International Journal of Quantum Chemistry, 60(4), 809-820.

Ortega-Castro, J., Hernandez-Haro, N., Timon, V., Sainz-Diaz, C.I., and Hernandez-Laguna, A. (2010) High-pressure behavior of 2M(1) muscovite. American Mineralogist, 95(2-3), 249-259.

Ottonello, G., Civalleri, B., Ganguly, J., Perger, W.F., Belmonte, D., and Zuccolini, M.V. (2010) Thermo-chemical and thermo-physical properties of the high-pressure phase anhydrous B ($Mg_{14}Si_5O_{24}$): An ab-initio all-electron investigation. American Mineralogist, 95(4), 563-573.

555 Ottonello, G., Civalleri, B., Ganguly, J., Zuccolini, M.V., and Noel, Y. (2009a) Thermophysical properties of
556 the α–β–γ polymorphs of Mg2SiO4: a computational study. Physics and Chemistry of Minerals,
557 36(2), 87-106.
558 Ottonello, G., Zuccolini, M.V., and Civalleri, B. (2009b) Thermo-chemical and thermo-physical properties
559 of stishovite: An ab-initio all-electron investigation. CALPHAD: Computer Coupling of Phase
560 Diagrams and Thermochemistry, 33(3), 457-468.
561 Pascale, F., Zicovich-Wilson, C.M., Gejo, F.L., Civalleri, B., Orlando, R., and Dovesi, R. (2004) The
562 calculation of the vibrational frequencies of crystalline compounds and its implementation in the
563 CRYSTAL code. Journal of Computational Chemistry, 25(6), 888-897.
564 Prencipe, M., Pascale, F., Zicovich-Wilson, C.M., Saunders, V.R., Orlando, R., and Dovesi, R. (2004) The
565 vibrational spectrum of calcite (CaCO3): an ab initio quantum-mechanical calculation. Physics and
566 Chemistry of Minerals, 31(8), 559-564.
567 Prencipe, M., Scanavino, I., Nestola, F., Merlini, M., Civalleri, B., Bruno, M., and Dovesi, R. (2011) High-
568 pressure thermo-elastic properties of beryl (Al4Be6Si12O36) from ab initio calculations, and
569 observations about the source of thermal expansion. Physics and Chemistry of Minerals, 38(3), 223-
570 239.
571 Putnis, A. (1992) An introduction to mineral sciences. 457 p. Cambridge University Press, Cambridge, UK.
572 Robie, R.A., Hemingway, B.S., and Wilson, W.H. (1976) Heat capacities of calorimetry conference copper
573 and of muscovile $KAl_2(AlSi_3)O_{10}(OH)_2$, pyrophyllite $Al_2Si_4O_{10}(OH)_2$, and illite
574 $K_3(Al_7Mg)(Si_{14}Al_2)O_{40}(OH)_8$ between 15 and 375 K and their standard entropies at 298.15K. Journal
575 of Research of the U.S. Geological Survey, 4(6), 631-644.
576 Rothbauer, R. (1971) Untersuchung eines $2M_1$-muskovits mit neutronenstrahlen. Neues Jahrbuch fuer
577 Mineralogie, Monatshefte, 143-154.
578 Saito, M., and Yamaguchi, N. (2009) Manufacture of mica product for electronic product, involves
579 immersing coarse crushing material obtained by pulverizing raw-ore stone of muscovite in acid
580 solution and peeling. Yamaguchi Unmo Kogyosho Kk.
581 Shanno, D.F. (1970) Conditioning of quasi-Newton methods for function minimization. Mathematics of
582 Computation, 24, 647-656.

Stixrude, L. (2002) Talc under tension and compression: Spinodal instability, elasticity, and structure. Journal of Geophysical Research-Solid Earth, 107(B12).

Tosoni, S., Pascale, F., Ugliengo, P., Orlando, R., Saunders, V.R., and Dovesi, R. (2005) Quantum mechanical calculation of the OH vibrational frequency in crystalline solids. Molecular Physics, 103(18), 2549-2558.

Ulian, G., Tosoni, S., and Valdrè, G. (2013) Comparison between Gaussian-type Orbitals and Plane Wave *ab initio* DFT modeling of layered silicates: Talc mineral as model system. Journal of Chemical Physics, 139(20), 204101.

-. (2014) The compressional behaviour and the mechanical properties of talc [$Mg_3Si_4O_{10}(OH)_2$]: a density functional theory investigation. Physics and Chemistry of Minerals, 41(8), 639-650, DOI: 10.1007/s00269-014-0677-x.

Ulian, G., and Valdrè, G. (2014) Density Functional investigation of the thermophysical and thermochemical properties of Talc [$Mg_3Si_4O_{10}(OH)_2$]. Physics and Chemistry of Minerals, in press, DOI: 10.1007/s00269-014-0708-7.

599 **LIST OF TABLES**

Table 1. Calculated and experimental unit-cell and internal geometry of Muscovite.

	Present work DFT/B3LYP-D*	Experimental XRD*	Experimental XRD data ranges§	Neutron Diffraction†	DFT PBE‡
Lattice parameters					
a (Å)	5.1974	5.1579	5.174-5.226	5.1999	5.187
b (Å)	9.0389	8.9505	8.976-9.074	9.0198	9.006
c (Å)	19.8444	20.071	19.875-20.097	19.945	20.148
α (°)	90.27	90.00	90.00	90.00	90.00
β (°)	96.23	95.75	95.59-95.84	95.81	95.44
γ (°)	89.88	90.00	90.00	90.00	90.00
½csinβ	9.366	9.985	9.890-9.996	9.9213	10.029
Volume (Å^3)	926.74	921	926-945.4	930.66	936.999
Mean bond lengths (Å)					
O-H	0.961	-	0.95	-	0.974
Si-O	1.634	1.647	1.64	1.642	1.651
Al(T)-O	1.741	-	-	-	1.757
Al(Oc)-O(a)	1.937	1.921	1.927-1.94	1.939	1.934
Al(Oc)-O(h)	1.919	1.935	1.911	1.939	1.918
K-O_{outer}	3.380	3.368	3.272-3.373	3.329	3.427
K-O_{inner}	2.798	2.848	2.832-2.934	2.863	2.759
ΔK	0.582	0.520	0.426-0.509	0.466	0.6680
TOT structure					
Tetrahedral rotation (°)	12.2	11.8	10.3-11.3	10.39	14.6
Volume (T) Si,Al (Å^3)	2.222, 2.697	2.25	-	2.265	2.273, 2.774
Volume (Oc) (Å^3)	9.345	9.15	-	9.518	9.386
T thickness (Å)	2.248	2.234	2.262	2.224	2.277
Oc thickness (Å)	2.086	2.081	2.083	2.102	2.093
I thickness (Å)	3.260	3.436	3.375	3.125	3.361

***** data from (Guggenheim et al., 1987) $K_{1.00}Na_{0.03}Ca_{0.01}(Al_{1.93}Fe_{0.01}Mn_{0.01})(Al_{0.91}Si_{3.09})O_{10}(OH)_{1.88}F_{0.12}$

§ data collected from different sources (Burnham and Radoslovich, 1964): $K_{0.66}Na_{0.34}Al_2(AlSi_3)O_{10}(OH)_2$; (Rothbauer, 1971): $K_{0.85}Na_{0.1}(Al_{1.81}Fe^{2+}_{0.14}Mg_{0.12})(Al_{0.9}Si_{3.1})O_{9.8}(OH)_2$; (Catti et al., 1989): $K_{0.86}Na_{0.11}(Al_{1.93}Fe_{0.07}Mg_{0.02})(Al_{0.92}Si_{3.08})O_{10}(OH)_2$; (Catti et al., 1994a): $K_{0.90}Na_{0.07}(Al_{1.63}Fe_{0.23}Mg_{0.16}Ti_{0.03})(Al_{0.80}Si_{3.20})O_{10}(OH)_2$; (Brigatti et al., 1998): different compositions; (Mookherjee and Redfern, 2002): $K_{0.95}Na_{0.05}(Al_{0.76}Fe_{0.14}Mg_{0.10})_2(Al_{0.75}Si_{3.25})O_{10}(OH_{1.96}F_{0.04})$.

† data from neutron diffraction experiments at 20K (Gatta et al., 2011).

‡ theoretical data from (Hernandez-Haro et al., 2013)

600
601
602
603
604
605
606
607
608
609
610
611

Table 2. Simulated Muscovite unit-cell parameters at different volumes.

P_{st} (GPa)	$P_{BM\text{-}III}$ (GPa)	Volume (Å^3)	a (Å)	b (Å)	c (Å)	α (°)	β (°)	γ (°)
-1.24	-1.33	948.2	5.2149	9.0745	20.1613	90.24	96.36	89.89
-0.74	-0.75	938.3	5.2072	9.0587	20.0138	90.26	96.30	89.89
-0.14	-0.11	928.5	5.1990	9.0421	19.8699	90.27	96.25	89.88
-0.03	0.01	926.7	5.1974	9.0389	19.8444	90.27	96.23	89.88
0.53	0.58	918.8	5.1903	9.0246	19.7305	90.28	96.20	89.88
1.29	1.34	909.1	5.1811	9.0061	19.5953	90.29	96.15	89.88
2.13	2.16	899.4	5.1713	8.9866	19.4646	90.29	96.10	89.87
3.05	3.06	889.9	5.1610	8.9661	19.3384	90.30	96.05	89.87
4.05	4.03	880.4	5.1502	8.9446	19.2164	90.30	96.01	89.87
5.12	5.08	870.9	5.1389	8.9220	19.0987	90.30	95.96	89.86
6.27	6.22	861.5	5.1270	8.8987	18.9844	90.30	95.92	89.86
7.49	7.45	852.2	5.1148	8.8746	18.8734	90.31	95.87	89.85
8.77	8.77	843.0	5.1023	8.8499	18.7659	90.31	95.83	89.85
10.13	10.20	833.8	5.0893	8.8245	18.6604	90.31	95.78	89.84

Note: P_{st} values were obtained from 3-order polynomial fitting (p-fit) and $P_{BM\text{-}III}$ data from 3rd-order Birch-Murnaghan fitting (BM3).

Table 3. Comparison on theoretical and experimental BM3 results

	Present work	**Experimental XRD**	**Theoretical DFT/PBE**
T = 0 K			
K_T (GPa)	64.2 ± 1.2	-	59.81
K_T'	7.98 ± 0.33	-	6.96
V_0 (Å^3)	926.86 ± 0.38	-	-
T = 573 K			
K_T (GPa)	55.52 ± 1.29	55.1	-
K_T'	8.07 ± 0.32	-	-
V_0 (Å^3)	950.2 ± 0.6	938.0	-
T = 723 K			
K_T (GPa)	53.08 ± 1.42	51.1	-
K_T'	8.20 ± 0.33	-	-
V_0 (Å^3)	956.1 ± 0.8	944.1	-
T = 873 K			
K_T (GPa)	50.62 ± 1.56	48.9	-
K_T'	8.33 ± 0.36	-	-
V_0 (Å^3)	962.4 ± 1.0	952.5	-

Notes: experimental and theoretical values are taken from the works of Comodi et al. (2002) and Ortega-Castro et al. (2010), respectively.

FIGURE CAPTIONS

Figure 1. Schematic structure of ideal muscovite, viewed **(**a) from [100] and (b) from [001] directions: embedding of one interlayer I in between two TOT layers, each one of which consists of one octahedral sheet O sandwiched by two tetrahedral sheets T. (c) The local structure of the interlayer potassium ions, where 12 oxygen atoms in the first shell are interlayer atom, while Si and Al atoms are located in the centers of O tetrahedrons.

Figure 2. Stick and ball representation of the DFT optimized muscovite model viewed (a) from [100] and (b) from [001] directions.

Figure 3. (a) $E_{st}(V)$ in Hartree units and (b) $P(V)$ plots of muscovite obtained from ab initio calculations. The dashed lines helps in distinguishing compression regime (on the left) and expansion (on the right).

Figure 4. Ab initio pressure effects on muscovite unit-cell volume and axis lengths. The theoretical athermal results has been compared to those of Ortega-Castro et al. (2010).

Figure 5. (a) Grüneisen's parameters (γ) at P = 0 GPa as a function of frequency (ν). The dashed line represents the mean of the mode-γ. (b) Contributions to the zero total pressure of the static (P_{st}), zero point (P_{zp}) and thermal (P_{th}) pressures.

Figure 6. (a) $V(P)$ plot of muscovite compressional behavior at 298K compared to powder XRD data (Comodi et al., 2002; Curetti et al., 2006) and (b) $V(P,T)$ three-dimensional plot obtained with DFT/B3LYP-D*.

Figure 7. $\alpha_T K_T$ product (a) and α_T (b) calculated for muscovite at selected pressures. (c) isochoric (dashed lines) and isobaric (solid lines) heat capacities, compared to experimental calorimetric data (Robie et al., 1976).

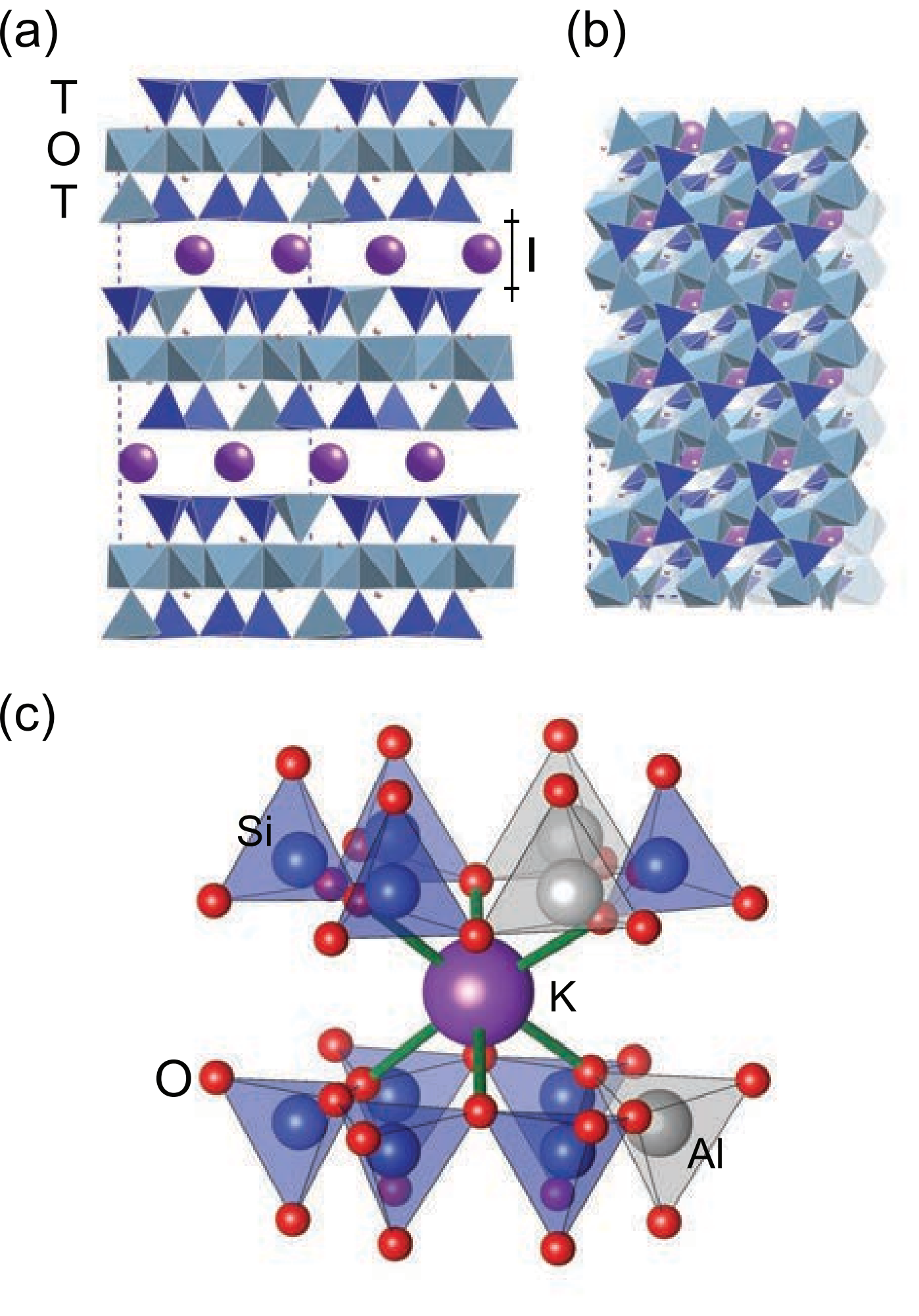
(a)
T
O
T
I
(b)
(c)
Si
K
O
Al

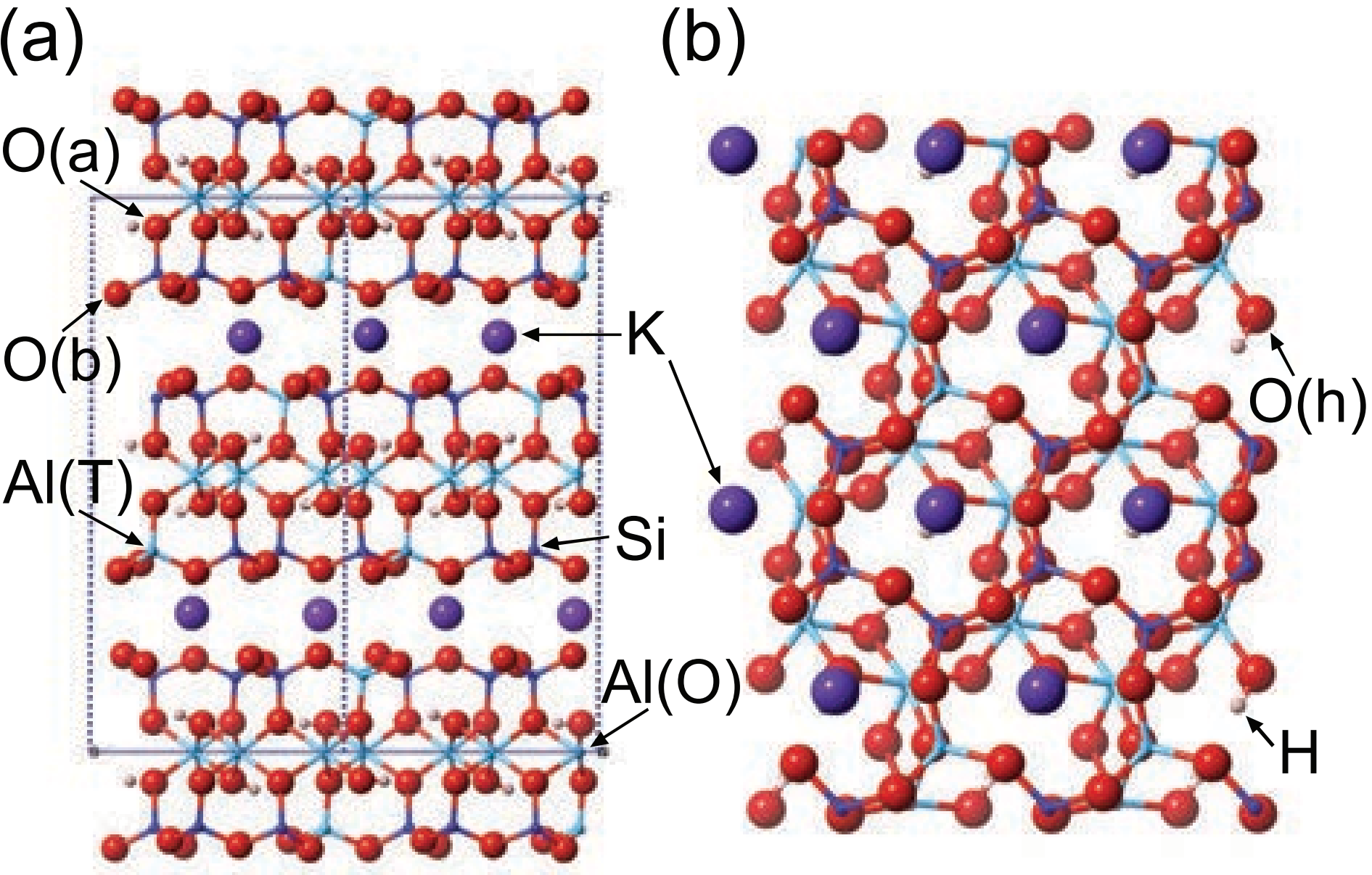
(a)
O(a)
O(b)
Al(T)
K
Si
Al(O)
(b)
O(h)
H

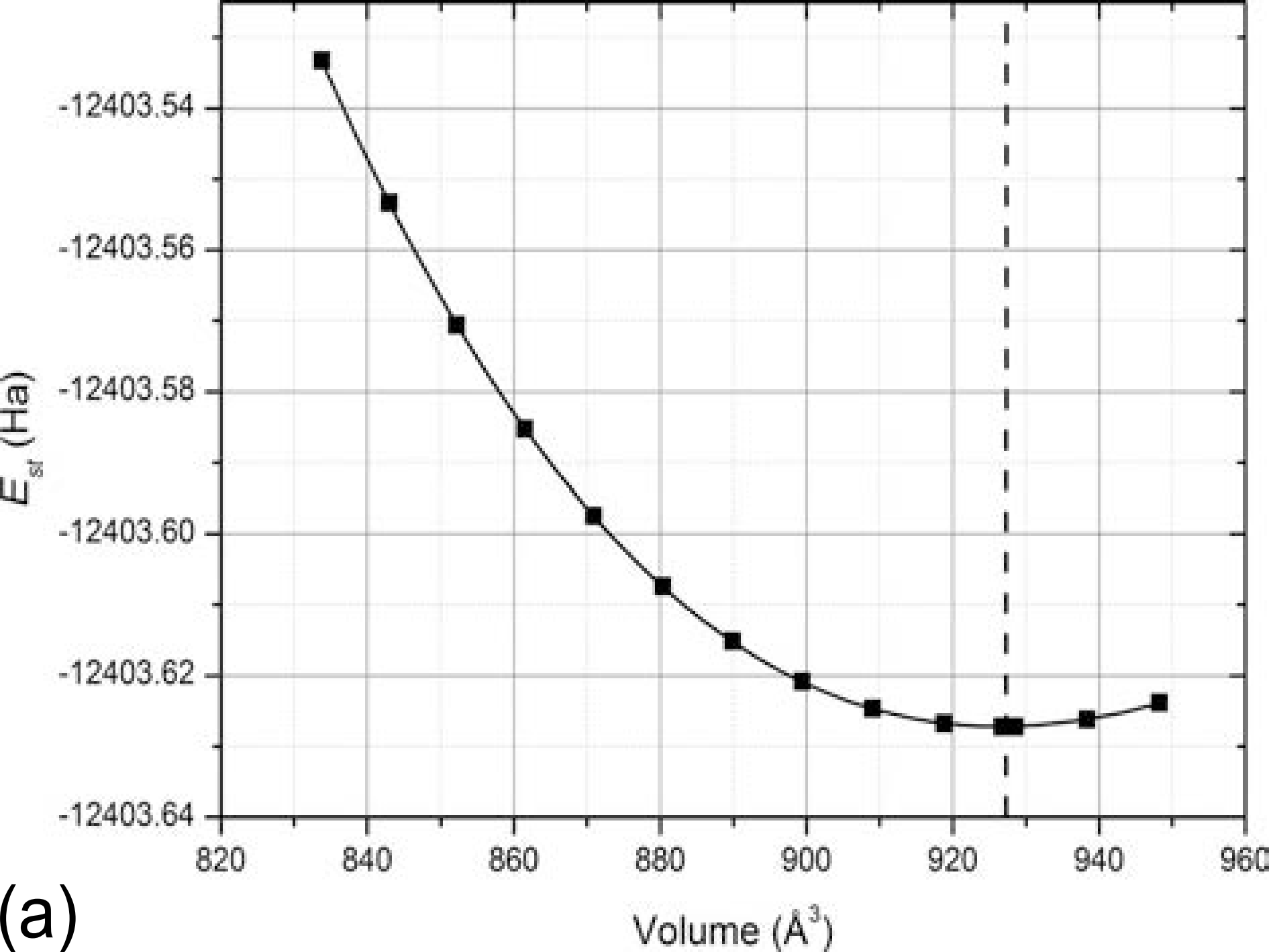
-12403.54
-12403.56
-12403.58
-12403.60
-12403.62
-12403.64
E_{sf} (Ha)
820
840
860
880
900
920
940
960
Volume (Å^3)

(a)

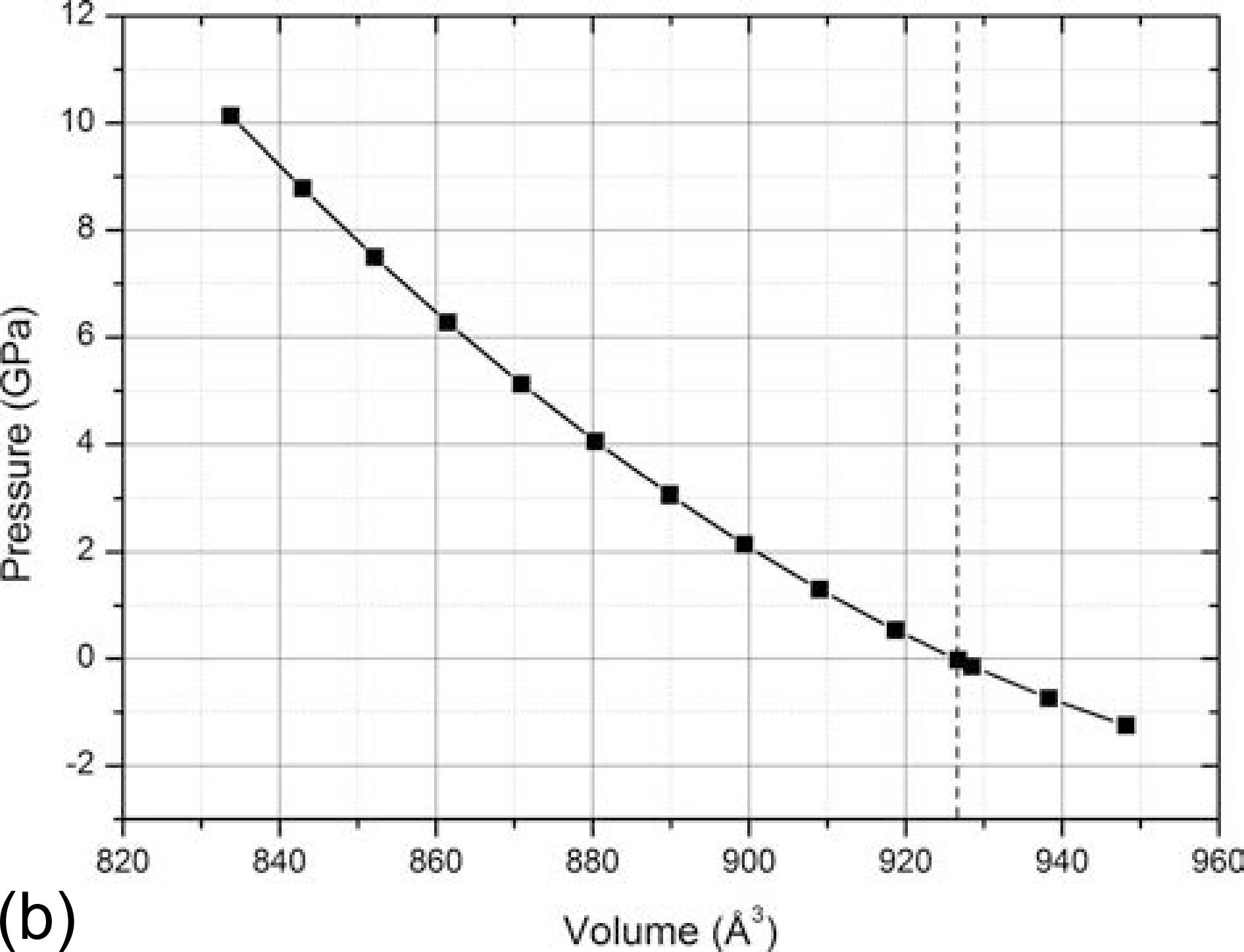
12
10
8
6
4
2
0
-2
Pressure (GPa)
820
840
860
880
900
920
940
960
Volume (Å^3)

(b)

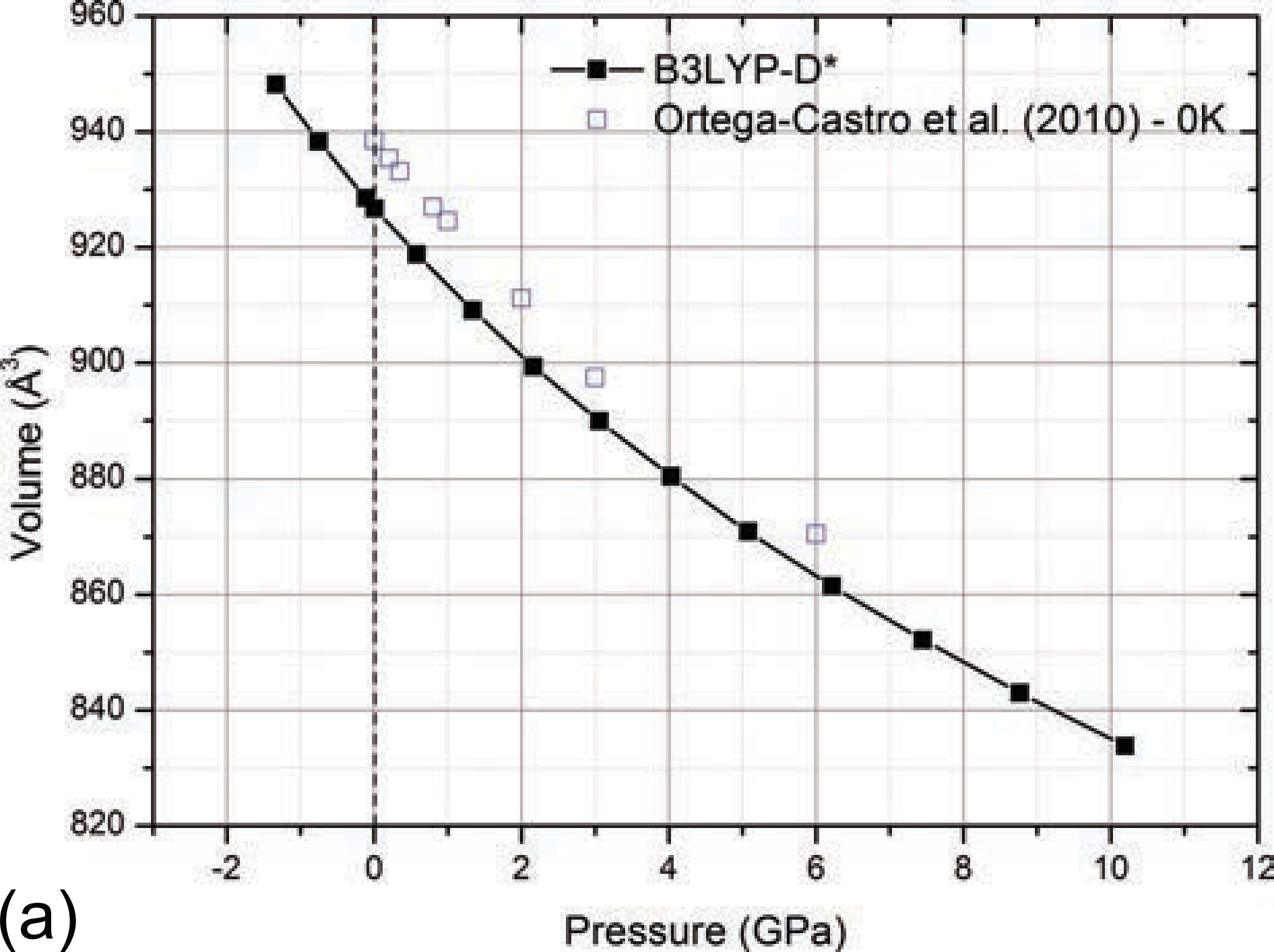
B3LYP-D*
Ortega-Castro et al. (2010) - 0K
Volume (Å^3)
Pressure (GPa)
960
940
920
900
880
860
840
820
-2
0
2
4
6
8
10
12

(a)

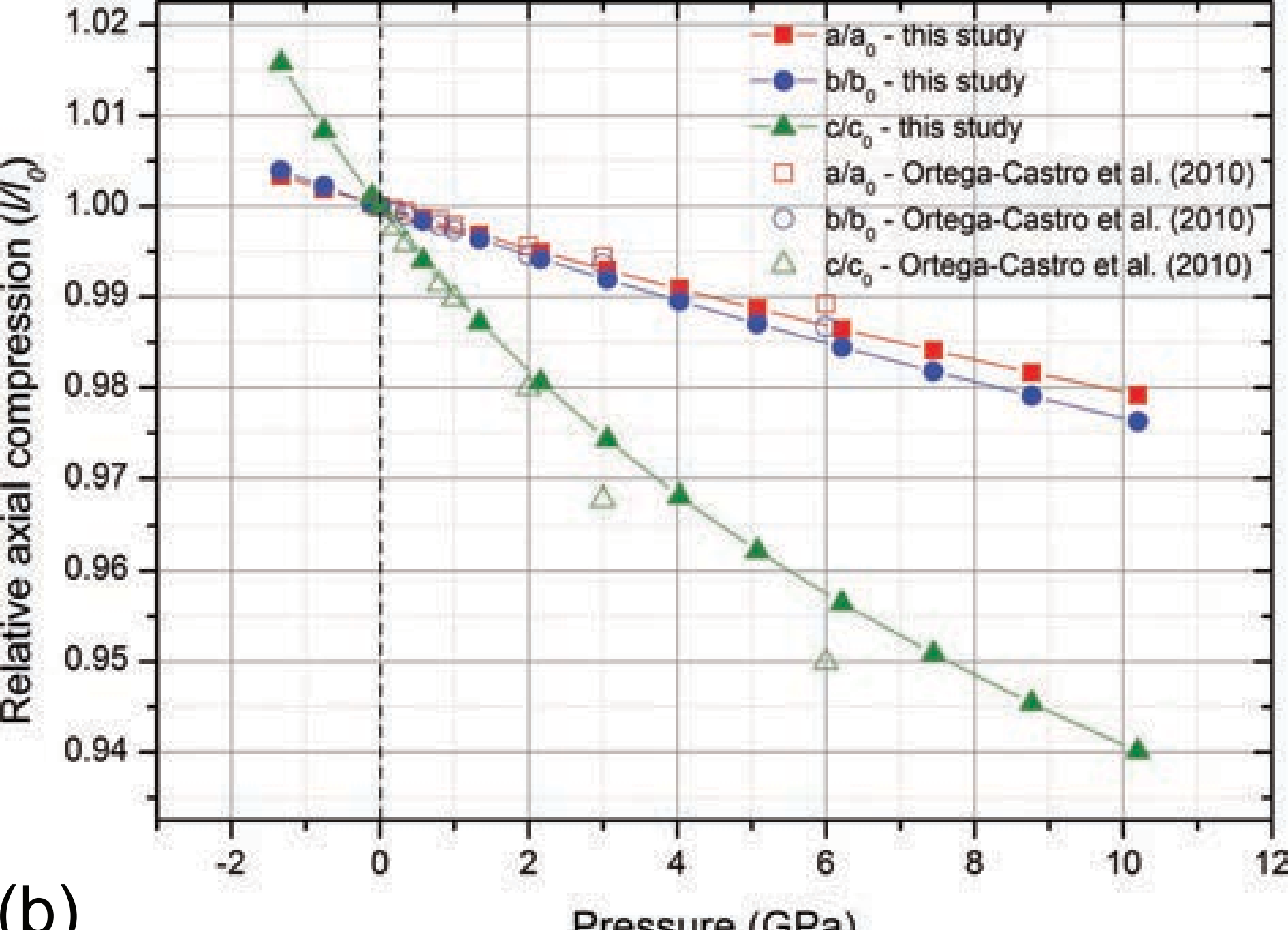
a/a0 - this study
b/b0 - this study
c/c0 - this study
a/a0 - Ortega-Castro et al. (2010)
b/b0 - Ortega-Castro et al. (2010)
c/c0 - Ortega-Castro et al. (2010)
Relative axial compression (l/l0)
Pressure (GPa)
1.02
1.01
1.00
0.99
0.98
0.97
0.96
0.95
0.94
-2
0
2
4
6
8
10
12

(b)

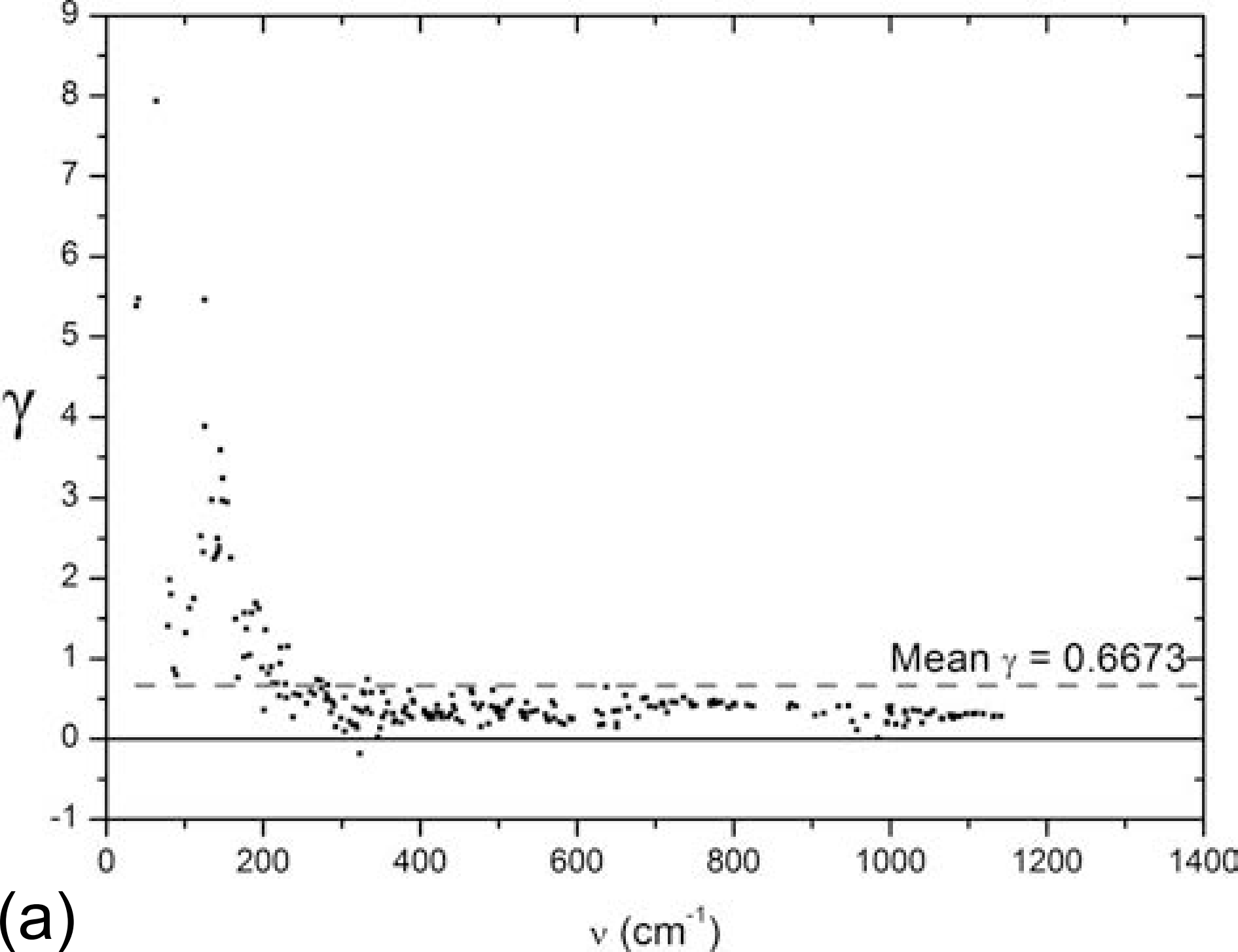
γ
Mean γ = 0.6673
ν (cm-1)
9
8
7
6
5
4
3
2
1
0
-1
0
200
400
600
800
1000
1200
1400

(a)

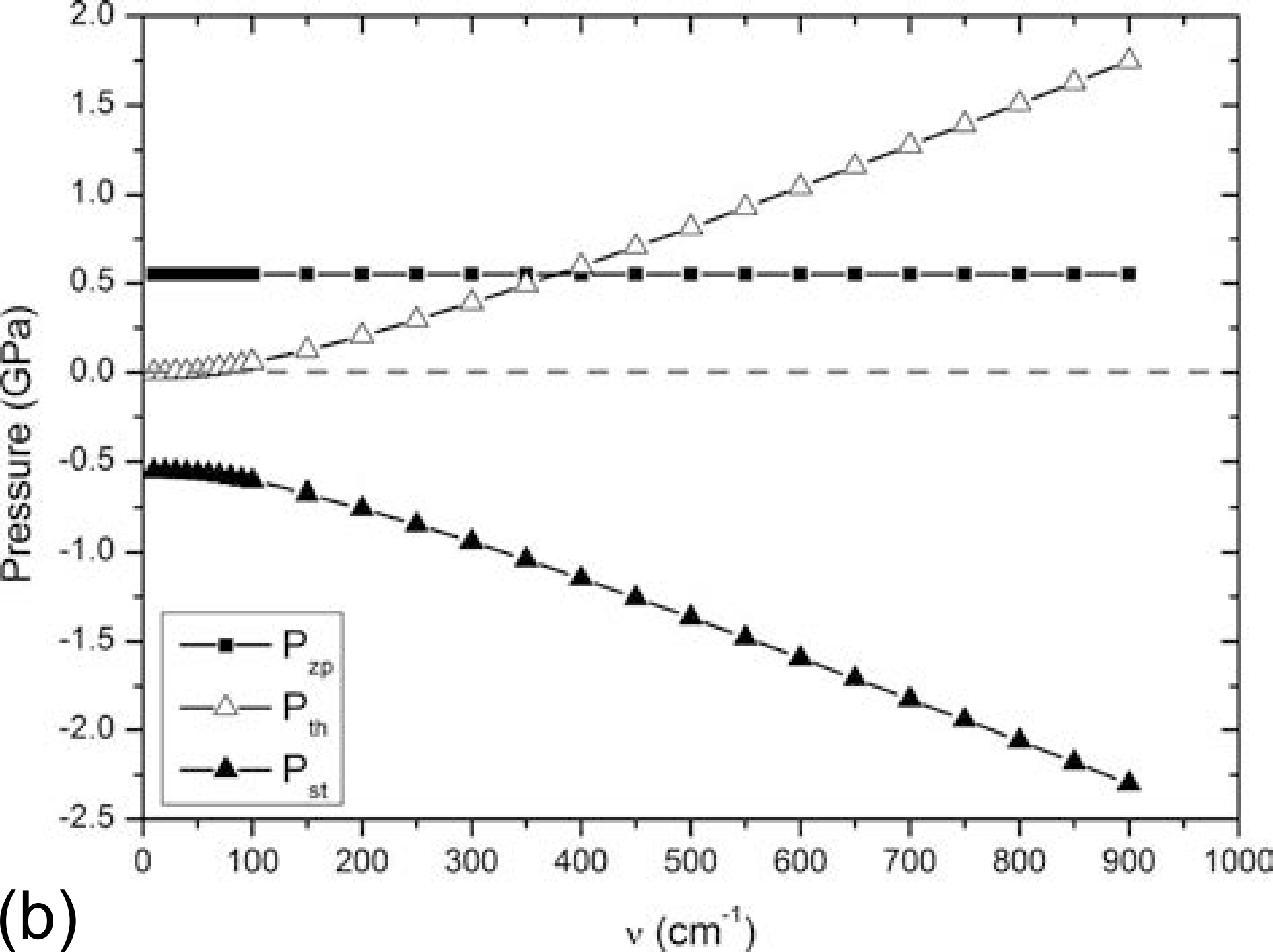
Pressure (GPa)
2.0
1.5
1.0
0.5
0.0
-0.5
-1.0
-1.5
-2.0
-2.5
0
100
200
300
400
500
600
700
800
900
1000
ν (cm-1)
Pzp
Pth
Pst

(b)

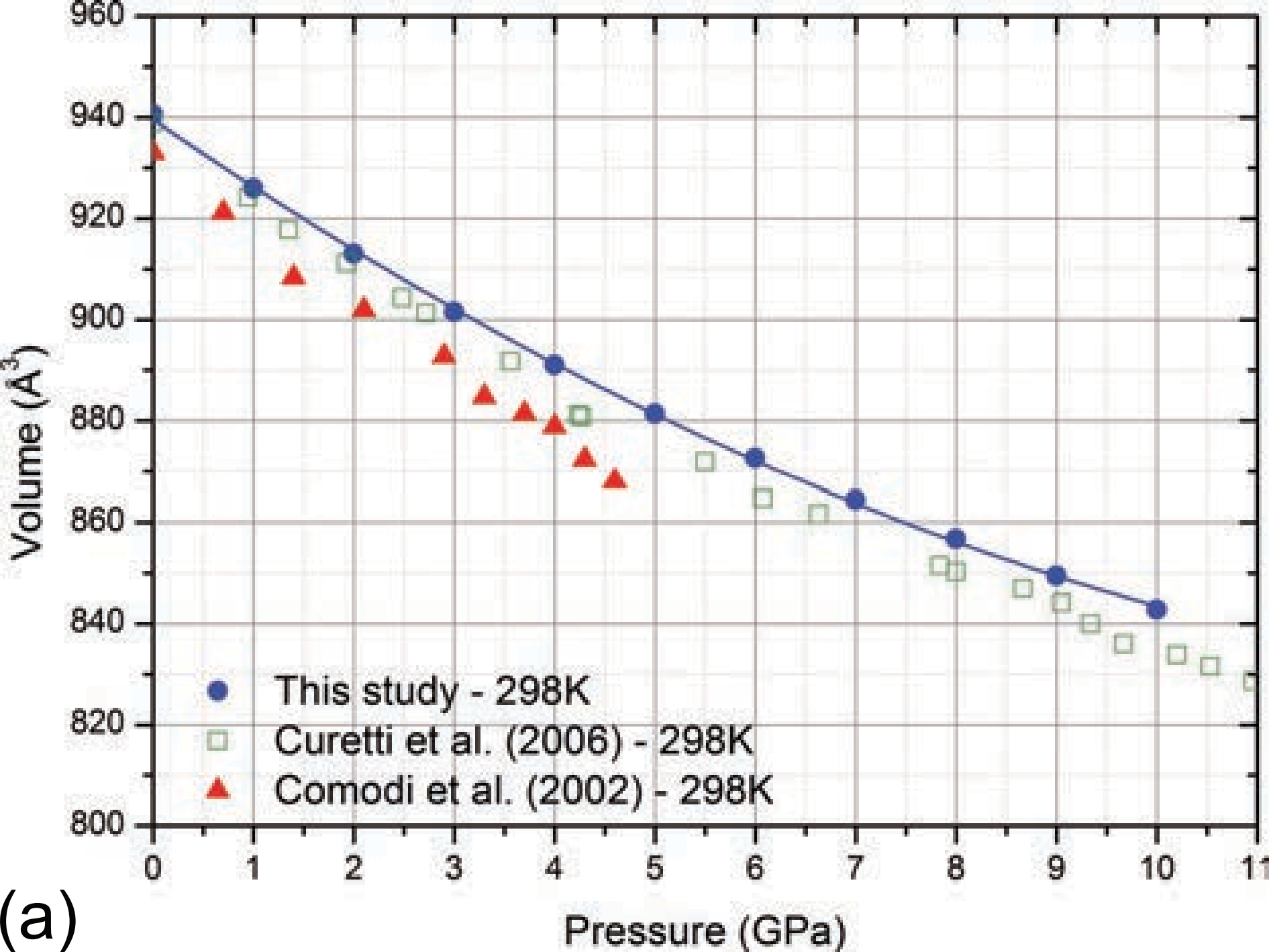
960
940
920
900
880
860
840
820
800
Volume (Å^3)
0
1
2
3
4
5
6
7
8
9
10
11
Pressure (GPa)
This study - 298K
Curetti et al. (2006) - 298K
Comodi et al. (2002) - 298K

(a)

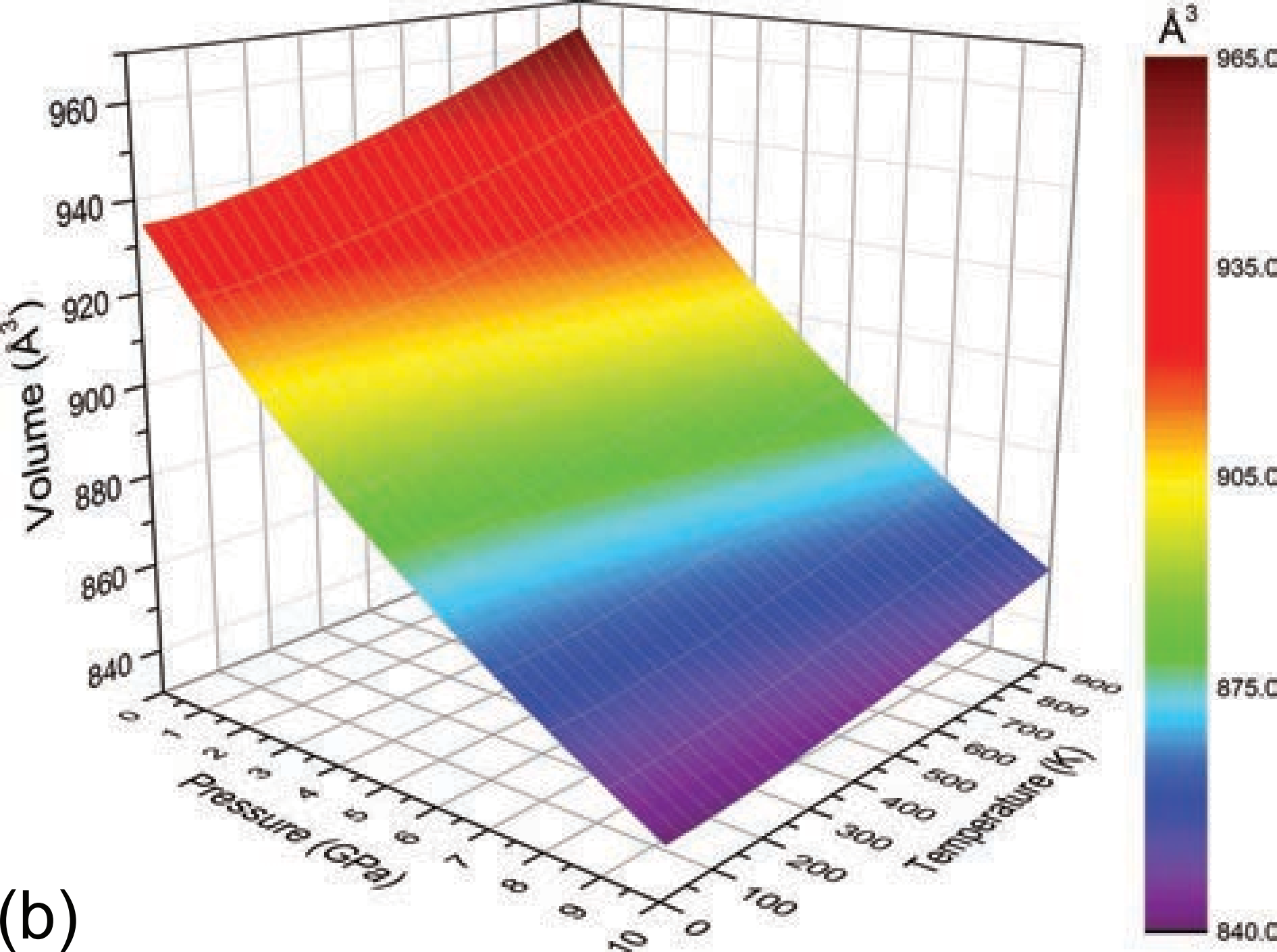
Volume (Å^3)
960
940
920
900
880
860
840
Pressure (GPa)
0
1
2
3
4
5
6
7
8
9
10
Temperature (K)
0
100
200
300
400
500
600
700
800
900
Å^3
965.0
935.0
905.0
875.0
840.0

(b)

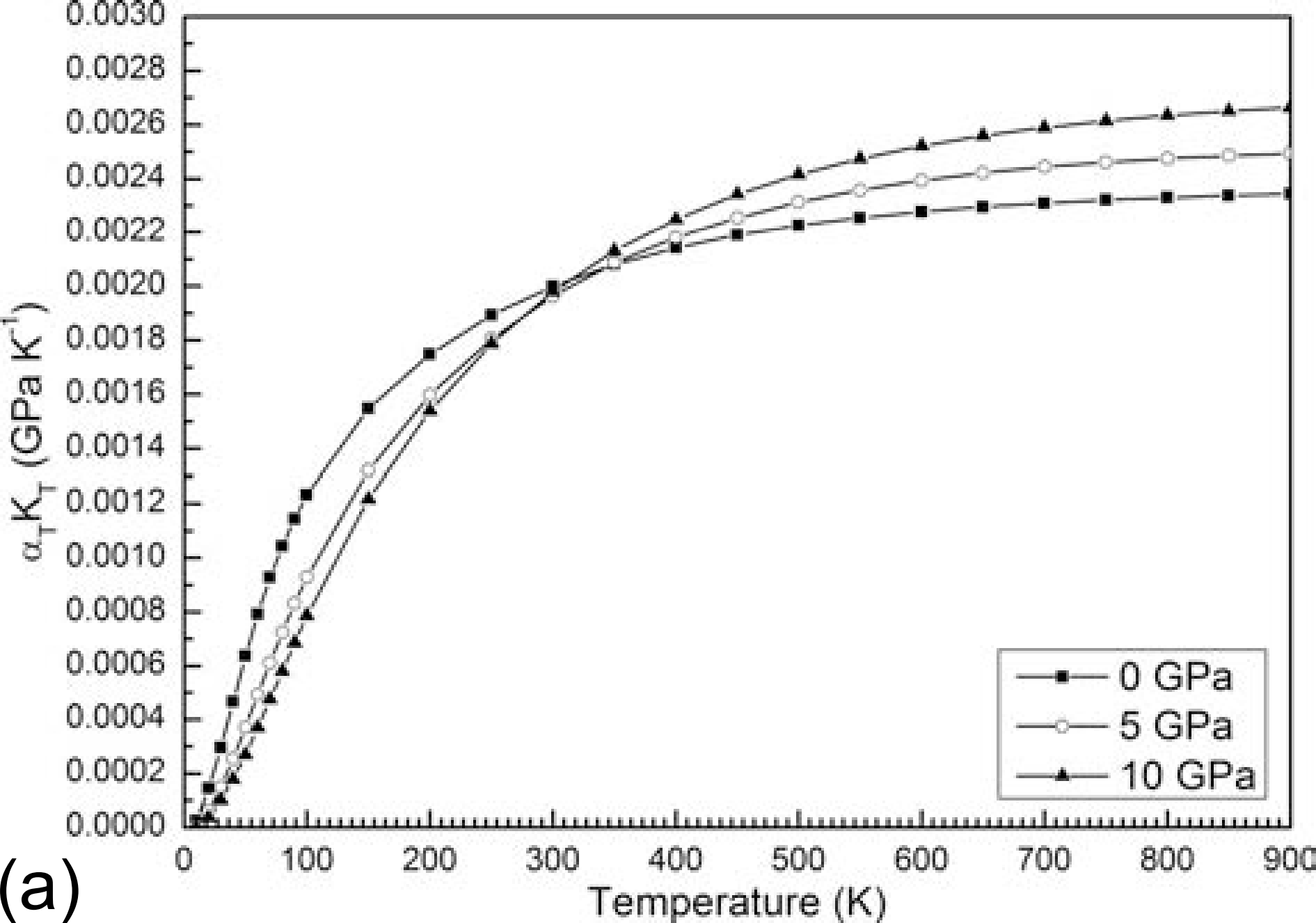
0.0030
0.0028
0.0026
0.0024
0.0022
0.0020
0.0018
0.0016
0.0014
0.0012
0.0010
0.0008
0.0006
0.0004
0.0002
0.0000
$\alpha_T K_T$ (GPa K^{-1})
0
100
200
300
400
500
600
700
800
900
Temperature (K)
0 GPa
5 GPa
10 GPa

(a)

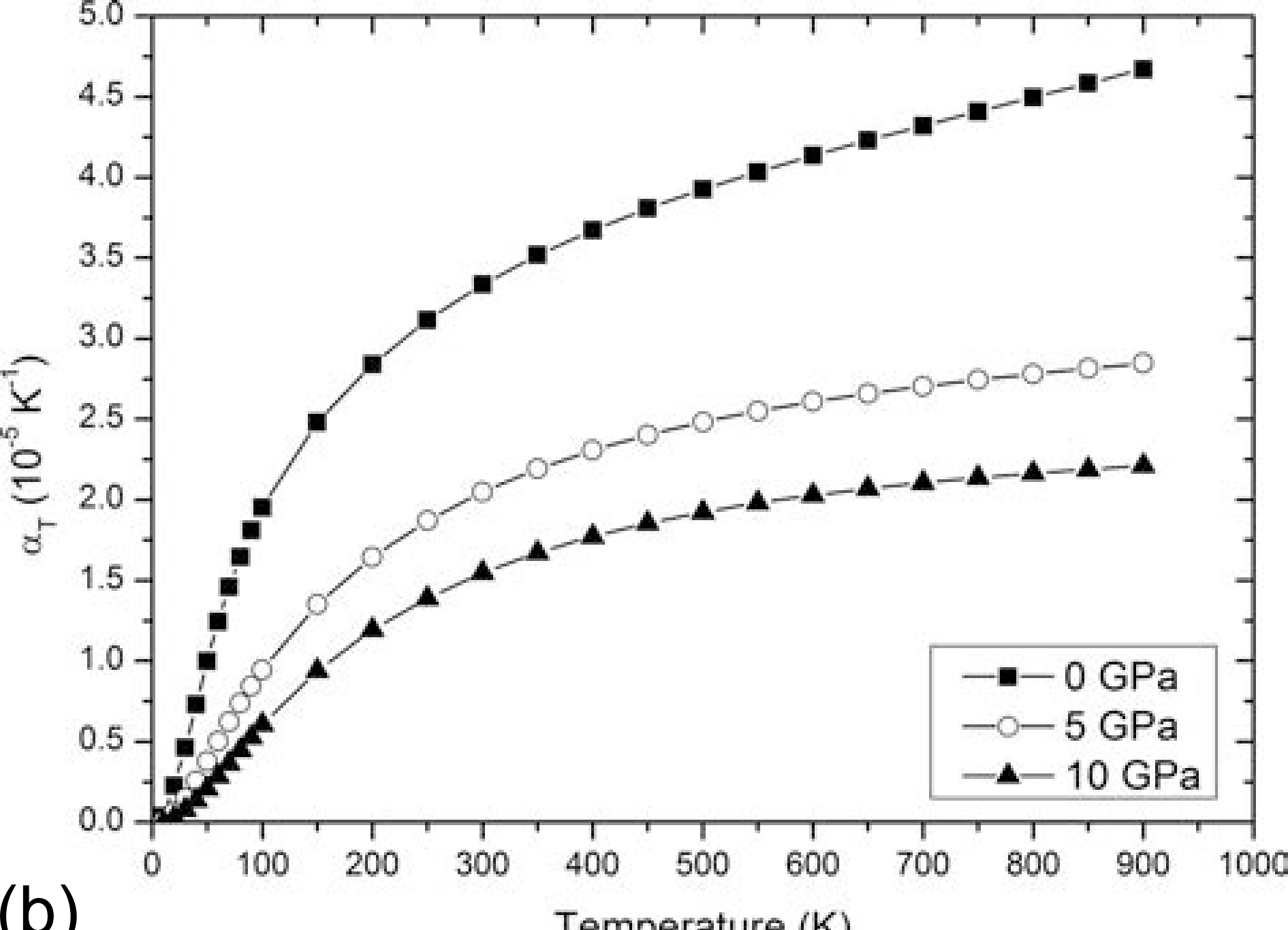
5.0
4.5
4.0
3.5
3.0
2.5
2.0
1.5
1.0
0.5
0.0
α_T (10^{-5} K^{-1})
0
100
200
300
400
500
600
700
800
900
1000
Temperature (K)
0 GPa
5 GPa
10 GPa

(b)

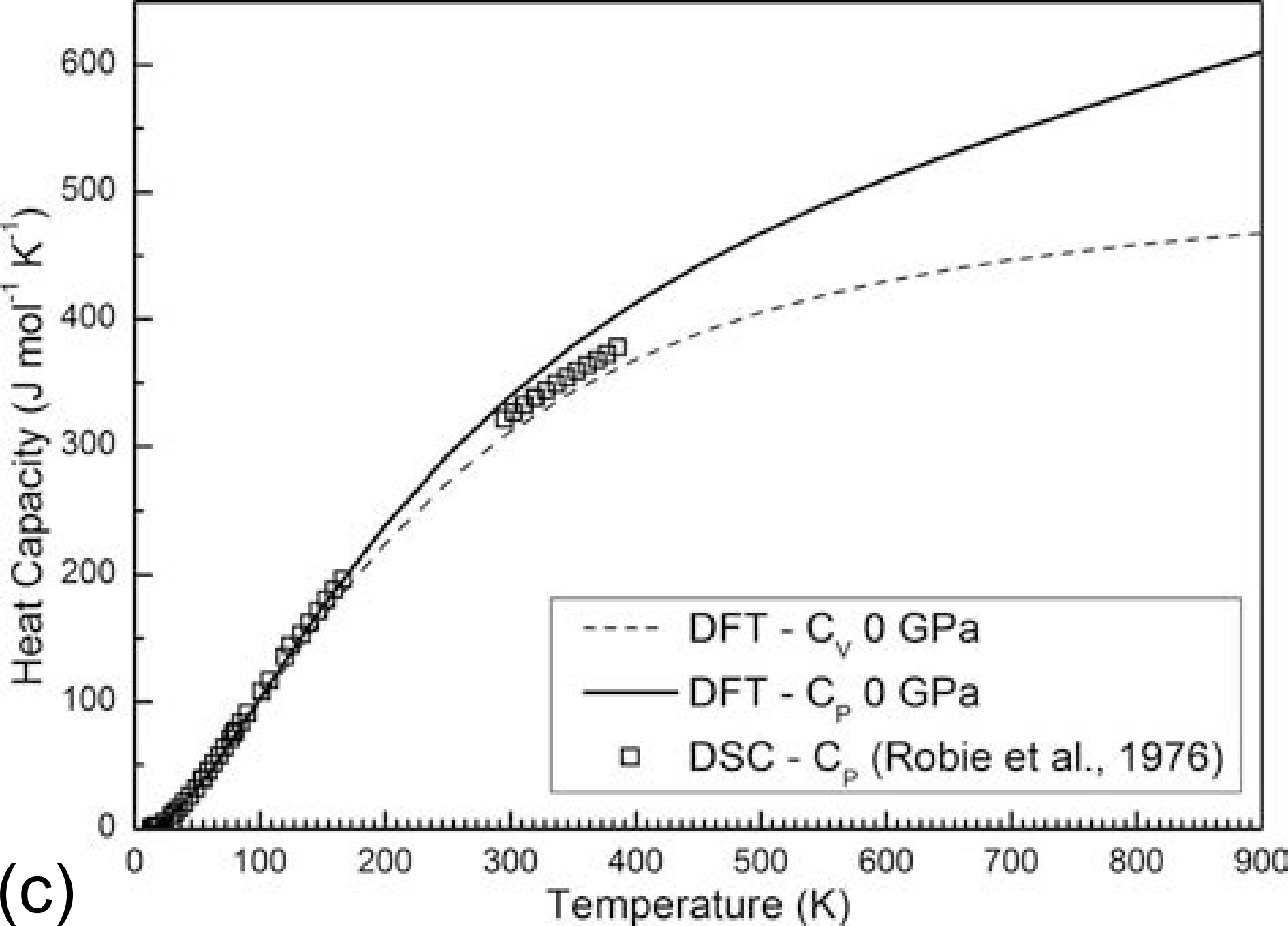
Heat Capacity (J mol-1 K-1)
Temperature (K)
0
100
200
300
400
500
600
700
800
900
DFT - CV 0 GPa
DFT - CP 0 GPa
DSC - CP (Robie et al., 1976)

(c)